The Canadian Mineralogist
Vol. 43, pp. 51-88 (2005)

CONTRASTING SEQUENCES OF METAPELITIC MINERAL-ASSEMBLAGES IN THE AUREOLE OF THE TILTED NELSON BATHOLITH, BRITISH COLUMBIA: IMPLICATIONS FOR PHASE EQUILIBRIA AND PRESSURE DETERMINATION IN ANDALUSITE–SILLIMANITE-TYPE SETTINGS

David R.M. PATTISON[§]

Department of Geology & Geophysics, University of Calgary, Calgary, Alberta T2N 1N4, Canada

James J. VOGL[§]

Department of Geological Sciences, University of Florida, Gainesville, Florida 32611, USA

Abstract

The Nelson Batholith is a *ca.* 1,800 km^2 Jurassic intrusive body in southeastern British Columbia surrounded by a contact aureole, 0.7–1.8 km wide, developed in graphitic argillaceous rocks that show only minor variations in bulk composition. Contrasting prograde sequences of mineral assemblages are developed around the aureole in a regular pattern, reflecting different pressures of contact metamorphism. The following assemblages are seen going from lower to higher pressure (all assemblages contain muscovite + biotite + quartz ± Mn-rich garnet): (1) cordierite-only assemblages, (2) mix of cordierite-only and cordierite + andalusite assemblages, locally with cordierite + K-feldspar and andalusite + K-feldspar assemblages at higher grade, (3) andalusite-only assemblages, with sillimanite + andalusite assemblages and locally sillimanite + K-feldspar assemblages at higher grade, (4) staurolite-only assemblages, (5) staurolite ± andalusite assemblages, with sillimanite-bearing and locally sillimanite + K-feldspar assemblages at higher grade. The higher-pressure sequences with staurolite ± andalusite are restricted to the aureole surrounding the east half of the batholith, whereas the lower-pressure cordierite ± andalusite are restricted to the aureole surrounding the west half of the batholith and its northern and southern tips. The sequences of mineral assemblages correspond closely to the facies series of Pattison & Tracy (1991) and are interpreted to represent a series of approximately isobaric metamorphic field-gradients below the Al_2SiO_5 triple point, providing an excellent opportunity to evaluate thermodynamically calculated low-pressure phase equilibria in the metapelitic system. The total difference in pressure represented by the contrasting assemblages is about 1.0 kbar, showing that they are a sensitive measure of small differences in pressure within the stability field of andalusite. Thermobarometry results from the aureole are moderately consistent with the mineral assemblage constraints, but carry pressure uncertainties larger than the total range of pressure represented by the aureole's assemblages. Pressures of the intrusive rocks derived from hornblende barometry are scattered, and many do not agree with the pressure constraints from the aureole. The mineral-assemblage constraints indicate down-to-the-west post-metamorphic tilting of the batholith and aureole of about 10°, interpreted to be due to a combination of eastward thrusting of the Nelson Batholith over crustal-scale ramps during Cretaceous–Paleocene shortening and Eocene east-side-down normal motion on the Slocan Lake – Champion Lakes fault system that forms the western boundary of the batholith.

Keywords: Nelson Batholith, contact metamorphism, metapelites, phase equilibria, cordierite, andalusite, staurolite, geothermobarometry, hornblende barometry, tectonics, British Columbia.

Sommaire

Le batholite jurassique de Nelson, couvrant une superficie d'environ 1,800 km^2 dans le sud-est de la Colombie-Britannique, est entouré d'une auréole de contact entre 0.7 et 1.8 km de large, développée dans une roche argileuse à graphite sans variations importantes en composition. Des contrastes dans les séquences d'assemblages progrades de minéraux sont apparents autour du batholite; ces séquences définissent un agencement régulier, témoignant de différentes pressions lors du métamorphisme de contact. On rencontre les assemblages suivants en allant de pression plus faible à plus élevée (tous les assemblages contiennent muscovite + biotite + quartz ± grenat manganésifère): (1) assemblages à cordiérite seule, (2) mélange d'assemblages à cordiérite seule et cordiérite + andalousite, ici et là avec les assemblages cordiérite + feldspath potassique et andalousite + feldspath potassique à un niveau de pression plus élevé, (3) assemblages à andalousite seule, avec assemblages à sillimanite + andalousite et, localement, sillimanite + feldspath potassique à un niveau de pression plus élevé, (4) assemblages à staurolite seule, et (5)

[§] *E-mail addresses*: pattison@ucalgary.ca, jvogl@geology.ufl.edu

assemblages à staurolite ± andalousite, avec des assemblages à sillimanite ou à sillimanite + feldspath potassique à un niveau de pression plus élevé. Les séquences typiques de pression plus élevée, contenant les assemblages à staurolite ± andalousite, ne sont développées que dans l'auréole entourant la moitié est du batholite, tandis que les assemblages typiques de pression plus faibles, à cordiérite ± andalousite, ne le sont que dans l'auréole autour de la moitié ouest du batholite et ses extrémités nord et sud. Les séquences d'assemblages de minéraux correspondent à la série de faciès de Pattison et Tracy (1991), et représenteraient une série de gradients metamorphiques isobares en dessous du point triple Al_2SiO_5, fournissant ainsi une excellente occasion d'évaluer thermodynamiquement les équilibres de phases calculés à faible pression dans un système métapélitique. L'intervalle en pression représenté par ces séquences contrastantes serait de l'ordre de 1.0 kbar, ce qui prouve qu'elles offrent une mesure sensible de faibles différences en pression dans le champ de stabilité de l'andalousite. Les résultats thermobarométriques provenant de l'auréole concordent *grosso modo* avec les contraintes imposées par les séquences d'assemblages de minéraux, mais les incertitudes en pression dépassent l'intervalle total de pression indiquée par ces assemblages. Les pressions dérivées de la barométrie de la hornblende dans les roches intrusives sont éparses, et plusieurs montrent une discordance avec les pressions déduites de l'auréole. Les contraintes apportées par les assemblages de minéraux indiquent un basculement du batholite et de son auréole de 10° avec affaissement vers l'ouest, postérieur au métamorphisme; ce mouvement serait dû à une combinaison d'un chevauchement vers l'est du batholite de Nelson sur des rampes dans la croûte au cours d'un raccourcissement régional du crétacé au paléocène, et un mouvement normal éocène, avec le côté est affaissé, le long du système de failles Slocan Lake – Champion Lakes, qui délimite le batholite vers l'ouest.

(Traduit par la Rédaction)

Mots-clés: batholite de Nelson, métamorphisme de contact, métapélites, équilibre de phases, cordiérite, andalousite, staurolite, géothermobarométrie, barométrie fondée sur la hornblende, tectonique, Colombie-Britannique.

Introduction

The petrogenetic grid for metapelites has been one of Dugald Carmichael's career-long interests and plays a central role in his scheme of bathograds and bathozones (Carmichael 1978). Our paper concerns with the systematics and thermodynamic modeling of metapelitic phase-equilibria in the low-pressure part of P–T space below the Al_2SiO_5 triple point, corresponding to bathozones 1–3 of Carmichael's (1978) scheme. The emphasis is on intermediate-grade (amphibolite-facies) mineral assemblages involving combinations of cordierite, andalusite, staurolite, sillimanite, garnet and chlorite that are developed in rocks containing muscovite + biotite + quartz. The phase equilibria are difficult to model thermodynamically because of the compositional complexity of the minerals involved and the sensitivity of the calculated phase-equilibria to small changes in the thermodynamic parameters used (Pattison *et al.* 2002). The result is marked differences in thermodynamically predicted phase-relations at low pressure; see Figure 1 of Pattison *et al.* (1999) for a summary.

The P–T range represented by the above assemblages is *ca.* 500–650°C and *ca.* 2.0–4.5 kbar. Realistic uncertainties on P–T results from conventional and multi-equilibrium thermobarometry, taking account of random analytical errors and especially systematic errors related to thermodynamic models and assumptions about which parts of minerals were in equilibrium at peak conditions, are at least ±50°C and ±1 kbar. This covers most of the P–T region of interest, within which there are systematic variations in the mineral assemblages as a function of pressure and bulk composition (Pattison & Tracy 1991). Being able to thermodynamically model these phase equilibria therefore holds the potential for fine-scale estimation of pressure beyond that which thermobarometry can provide.

Because experimental data on the end members and mixing properties of several of the key phases are missing or incomplete, assemblages of minerals provide important constraints on thermodynamic models. The phase-equilibrium systematics found by Pattison & Tracy (1991) were based on repeated occurrences of mineral assemblages in contact aureoles. However, these were based on data from many different areas and bulk compositions, introducing uncertainty in separating the effects of P–T differences and bulk composition. The purpose of this paper is to present results from a single exceptional setting, the aureole surrounding the Nelson Batholith in southeastern British Columbia, in which phase relations for metapelitic compositions over a significant pressure-range below the triple point can be constrained in a single contact aureole. This unusual situation arises because of post-metamorphic tilting of the batholith and its aureole, which exposed contrasting prograde sequences of mineral assemblages developed in metapelitic rocks of restricted bulk-composition. The observed phase-equilibria are compared with the low-pressure facies series of Pattison & Tracy (1991) and with calculated phase-diagrams using current thermodynamic databases. Pressure constraints from the phase diagrams are compared against multi-equilibrium geothermobarometry-based estimates from the metapelites and Al-in-hornblende geobarometry of the intrusive rocks. The phase diagrams allow quantitative estimates of the amount of post-metamorphic tilting of the batholith and aureole, the tectonic implications of which are discussed at the end of the paper.

THE NELSON BATHOLITH AND AUREOLE

The Nelson Batholith is one of the largest of a suite of middle Jurassic plutons in southeastern British Columbia (*e.g.*, Archibald *et al.* 1983) (Fig. 1). It intrudes oceanic and ocean-margin rocks of the Quesnellia arc terrane that were thrust onto the North American continental margin in the early to middle Jurassic. The composite batholith ranges from tonalite to granite and comprises a northern mass, including the Mt. Carlyle Stock, of about 30×50 km^2 (referred to as the main body) and a 25 km long southern "tail" (Little 1960, Vogl & Simony 1992) (Fig. 1). Results of U–Pb dating indicate that the various phases of the batholith were intruded in the Jurassic between ~159 and 173 Ma (Parrish 1992, Sevigny & Parrish 1993, Ghosh 1995). Geophysical data show that the batholith is a tabular body with a flat-bottomed floor 2 to 7 km below present-day sea level (Cook *et al.* 1988). To the southwest of the Nelson Batholith is the smaller Bonnington Pluton, broadly of the same age and lithology. A Paleocene granite intrudes the southern part of the main mass of the Nelson Batholith (Sevigny & Parrish 1993) (Fig. 1).

The main body of the batholith and the northeastern margin of the tail intrude Upper Triassic rocks of the Slocan Group (Little 1960, Cairnes 1934) (Fig. 1). The rest of the tail intrudes Early Jurassic and Triassic rocks of the Ymir Group. The lower part of the Ymir Group is generally considered to correlate with the lithologically similar upper part of the Slocan Group (Little 1960). The Early Jurassic Archibald Formation of the Rossland Group, which crops out on the western flank of the Hall Syncline (Fig. 1), is considered to correlate with the upper Ymir Group (Little 1960).

Prior to intrusion of the Nelson Batholith, the region underwent contractional deformation during the juxtaposition of arc rocks of Quesnellia with the North American miogeocline. This Early to Middle Jurassic deformation produced thrust faults, two sets of folds, and widespread foliations. Regional Barrovian-style metamorphism developed in association with this deformation occurs in a narrow north–south-trending elongate culmination that reaches sillimanite grade near Kootenay Lake. The Nelson Batholith lies within the chlorite and biotite zones on the western flank of the regional metamorphic culmination (Archibald *et al.* 1983, and references therein) and was intruded during the final stages of the regional deformation and metamorphism (Little 1960, Fyles 1967, Vogl 1993). Following emplacement, the Nelson Batholith and aureole rode passively in the upper plate of deep-seated thrust faults that fed more easterly contractional structures (*e.g.*, Archibald *et al.* 1983, 1984). Contractional deformation gave way to horizontal extension and widespread normal faulting in the Eocene (*e.g.*, Carr *et al.* 1987, Parrish *et al.* 1988). The combination of Jurassic to Paleocene contractional deformation and Eocene extension led to tilting of the Nelson Batholith and aureole.

The western margin of the Nelson Batholith is bounded by the east-dipping Slocan Lake – Champion Lakes fault system (Fig. 1), a large Eocene system of normal faults that separates the batholith from the Valhalla metamorphic core complex (Carr *et al.* 1987, Parrish *et al.* 1988). Three closely spaced west-dipping faults (the Ainsworth faults), shown as a single fault-zone on Figure 1, occur between the eastern margin of the main body and Kootenay Lake (*e.g.*, Fyles 1967). The southern part of the westernmost fault coincides with the batholith – country-rock contact, on the basis of the juxtaposition of foliated granite with regionally metamorphosed staurolite-grade rocks (Fyles 1967). The Ainsworth faults are Jurassic thrust faults that were reactivated with normal motion in the Tertiary (Fyles 1967). The Midge Creek fault, a thrust fault likely related to the Ainsworth faults, coincides with the southeastern margin of the tail (Vogl & Simony 1992). Aside from these three perimeter zones, contacts are intrusive and provide suitable study-areas of the contact metamorphism.

Previous P–T work on the Nelson Batholith and aureole

The Nelson aureole, here defined by the outermost occurrence of porphyroblasts of cordierite, andalusite or staurolite, extends up to 1800 m from the intrusive contact and overprints the regional foliation (Fyles 1967, Childs 1968, Beddoe-Stephens 1981, Vogl 1993, this study). Mineral assemblages in the Nelson aureole have been reported by Drysdale (1917), Cairnes (1934), McAllister (1951), Hedley (1952), Fyles (1967), Crosby (1968), Childs (1968), Cox (1979), Beddoe-Stephens (1981), Brown & Logan (1988) and Vogl (1993). Many of the metapelitic rocks around the aureole contain andalusite, indicating emplacement pressures less than that of the Al_2SiO_5 triple point [*ca.* 3.8 kbar: Holdaway (1971), 4.5 kbar: Pattison (1992)]. Archibald *et al.* (1983) concluded that the aureole of the main (northern) part of the batholith is in bathozone 2 of Carmichael's (1978) scheme [2.2–3.5 kbar, using the triple point of Holdaway (1971)], with conditions possibly as high as bathozone 3 (≤4 kbar) adjacent to the southern tail of the batholith. Ghent *et al.* (1991) noted that low-Al hornblende in metabasic assemblages in the aureole of the southern part of the main batholith indicates pressures less than about 4 kbar.

Ghent *et al.* (1991) applied the Al-in-hornblende geobarometer to the intrusive rocks. Pressure estimates range from 3.1 to 6.4 kbar, with magmatic epidote occurring in a few samples that yielded the highest pressures. Spatial variations in pressure, although not very consistent, were attributed by Ghent *et al.* (1991) to a combination of regional tilts to the north and west related to Eocene normal faulting on the Slocan Lake Fault and upwarping of frozen-in isobaric surfaces due to late magmatic diapiric uprise. Our new data allow a test of

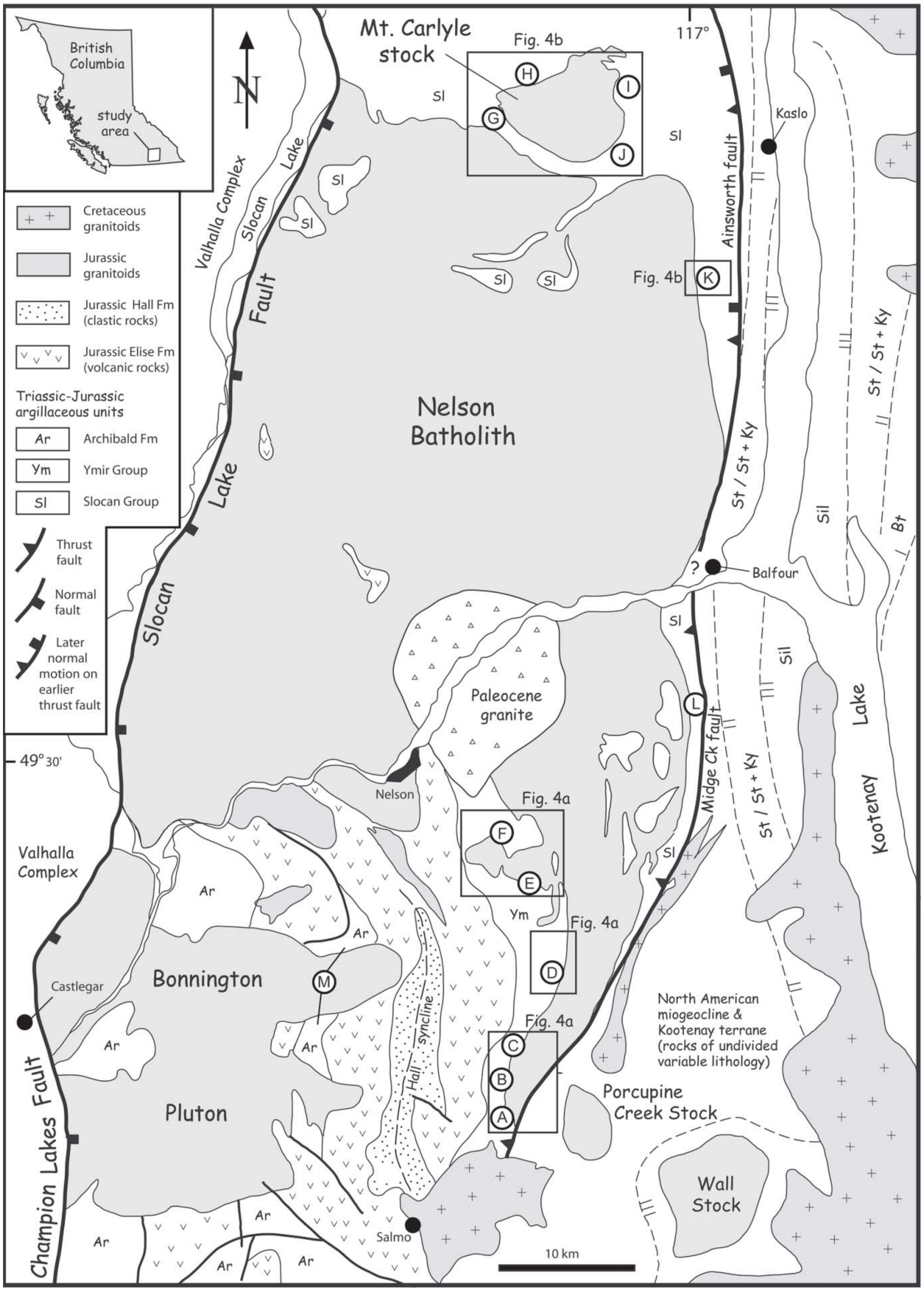

FIG. 1. Geological map of the Nelson Batholith and surrounding area. Letters in circles are the sampling areas discussed in the text.

this model and of the reliability of the hornblende geobarometer.

Lithology and Bulk Composition of Metapelites

The Ymir Group and Archibald Formation (south) and Slocan Group (north and east) are lithologically similar throughout the area, consisting of dark, graphitic, locally sulfide-rich argillites variably interbedded with quartzite, wacke and dark marble. Whole-rock X-ray fluorescence (XRF) analyses were done on 24 samples from around the aureole to check for compositional variability (see Fig. 2; locations of samples are shown in Fig. 4). The samples were obtained from the intermediate-grade (amphibolite-facies) porphyroblastic rocks that are the focus of this paper. Nineteen of the samples come from the Ymir Group and five come from the Slocan Group. Appendix 1 lists the results of the XRF analyses, and Table 1 provides some key compositional parameters.

Figure 2 shows the whole-rock compositions plotted in an AFM diagram projected from H_2O, quartz, average Nelson muscovite (Al/K = 3.24; Appendix 3), albite and anorthite components of plagioclase (Al/Na = 1 and Al/Ca = 2) and ilmenite (Fe/Ti = 1). Using this scheme, A = (Al – 3.24 K – Na – 2 Ca) / 2, and Fe = Fe^{2+} – Ti, assuming that all Fe is Fe^{2+}. Manganese and Fe^{3+} are ignored in the projection scheme. Low amounts of Fe^{3+} are anticipated because of the presence of ilmenite, pyrrhotite and graphite in most rocks, whereas the average MnO content of the Nelson rocks is 0.11 wt% (Appendix 1). The projection scheme is imperfect and not strictly thermodynamically valid (for example: Ca and Na are assumed to occur only in plagioclase, even though they are present as minor components of garnet and muscovite, respectively; Ca and Na are both assumed to be eliminated by projection from plagioclase, even though plagioclase is not uniform in composition in all rocks; and Ti is assumed to occur only in ilmenite, even though Ti is present as a minor component in biotite). Nevertheless, the projection scheme is successful in bringing the projected bulk-compositions close to the pertinent two-phase tie lines and three-phase regions for the measured mineral compositions in the same rocks [on average, within Mg/(Mg + Fe) = 0.02].

The data in Figure 2a show that the variability in A values is significant (mean 0.17; range –0.07 to 0.38, eliminating two extreme data), but that the variation in Mg/(Mg + Fe) is rather small (mean 0.45; range 0.40–0.50). Whether the range in A values reflects unrepre-

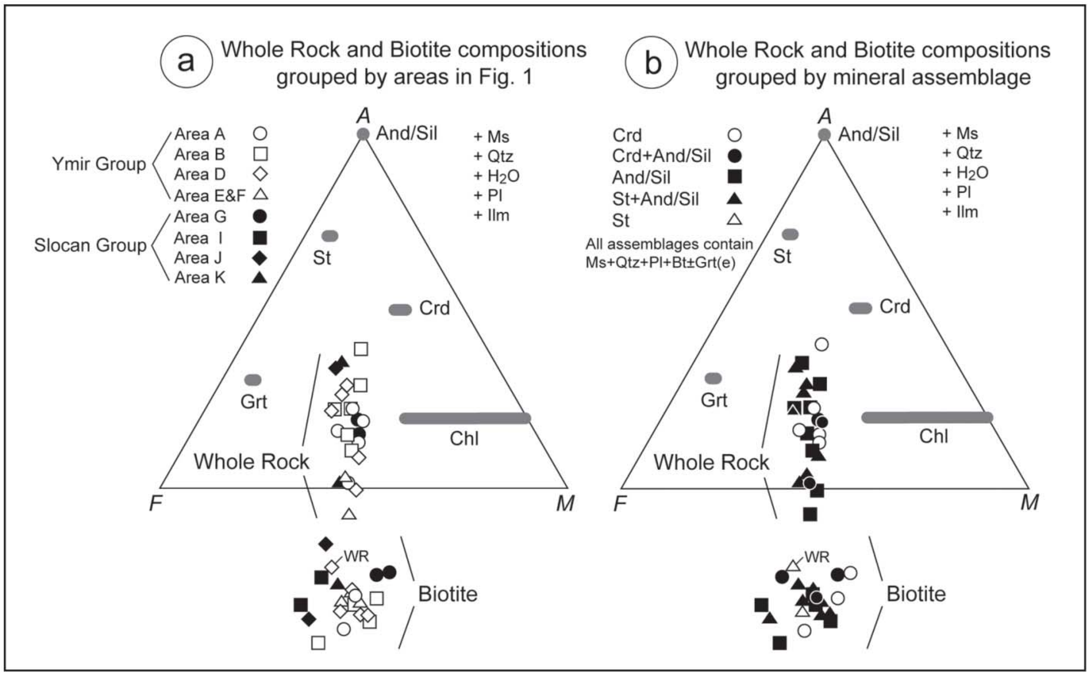

FIG. 2. AFM diagrams showing whole-rock and biotite compositions from around the aureole. The projection scheme is discussed in the text. The positions of staurolite, cordierite, garnet and chlorite are the average for the aureole. (a) Compositions grouped according to geographic locality and stratigraphic unit. (b) Compositions grouped according to mineral assemblage, using the symbols defined in Figure 4.

TABLE 1. SUMMARY OF WHOLE-ROCK AND MINERAL-COMPOSITION PARAMETERS RELEVANT TO ASSEMBLAGES IN THE AUREOLE OF THE NELSON BATHOLITH, BRITISH COLUMBIA

Area	Sample	SU	Dist.	Assemblage	WR1 Mg#	WR2 X_{Mn}	WR3 A	Bt1 Mg#	Bt2 Ti	Grt1 Mg#	Grt2 X_{Mn}	Grt3 X_{Ca}	St1 Mg#	St2 $X_{(Zn+Mn)}$	Crd Mg#
A	92-PC-20a	Ym	700	Crd	0.429	0.011	0.180	n.a.	n.a.	n.p.	n.p.	n.p.	n.p.	n.p.	alt'd
A	92-PC-19a	Ym	650	Crd	0.484	0.012	0.137	0.464	0.077	n.p.	n.p.	n.p.	n.p.	n.p.	0.583
A	92-PC-17	Ym	50	Crd-And	0.470	0.017	0.235	n.a.	n.a.	n.p.	n.p.	n.p.	n.p.	n.p.	n.a.
A	92-PC-27	Ym	50	Crd-And-Grt(e)	0.465	0.014	0.023	0.482	0.078	0.082	0.276	0.042	n.p.	n.p.	alt'd
	Average A				0.462	0.014	0.144	0.473	0.078						
B	03-OC-5b	Ym	700	Chl-Grt(e)	n.a.	n.a.	n.a.	n.a.	n.a.	0.107	0.235	0.039	n.a.	n.a.	n.a.
B	92-OC-10a	Ym	680	And	n.a.	n.a.	n.a.	0.484	0.095	n.p.	n.p.	n.p.	n.p.	n.p.	n.p.
B	92-OC-15a	Ym	630	Crd	0.494	0.012	0.424	0.525	0.098	n.p.	n.p.	n.p.	n.p.	n.p.	alt'd
B	92-OC-15b	Ym	630	And	n.a.	n.a.	n.a.	0.511	0.079	n.p.	n.p.	n.p.	n.p.	n.p.	n.p.
B	92-OC-9	Ym	550	And	0.491	0.013	0.268	n.a.	n.a.	n.p.	n.p.	n.p.	n.p.	n.p.	n.p.
B	03-OC-4	Ym	500	And-Sil-Grt(e)	0.413	0.054	0.287	n.a.	n.a.	n.a.	n.a.	n.a.	n.p.	n.p.	n.p.
B	92-OC-17	Ym	400	And-Sil-Grt(e)	0.465	0.022	0.149	n.a.	n.a.	n.a.	n.a.	n.a.	n.p.	n.p.	n.p.
B	92-OC-18c	Ym	350	And-Sil-Grt(e)	0.470	0.014	0.123	0.424	0.158	0.106	0.279	0.032	n.p.	n.p.	n.p.
B	03-OC-2b	Ym	20	And-Sil-Kfs	0.456	0.011	0.227	n.a.	n.a.	n.p.	n.p.	n.p.	n.p.	n.p.	n.p.
	Average B				0.465	0.021	0.246	0.486	0.108	0.107	0.257	0.036			
D	03-CW-5a	Ym	1500	Chl-Grt(e)	n.a.	n.a.	n.a.	n.a.	n.a.	0.140	0.463	0.088	n.a.	n.a.	n.a.
D	91-CW-8b	Ym	1400	St-And-Grt(e)	n.a.	n.a.	n.a.	0.496	0.090	0.120	0.157	0.056	0.160	0.049	n.p.
D	93-CW-4	Ym	1350	Grt(e)	n.a.	n.a.	n.a.	n.a.	n.a.	0.105	0.244	0.054	n.a.	n.a.	n.a.
D	93-CW-22	Ym	900	St-And-Grt(e)	0.403	0.010	0.238	0.492	0.089	0.128	0.125	0.044	0.155	0.041	n.p.
D	91-CW-9b	Ym	800	St-And-Grt(e)	n.a.	n.a.	n.a.	0.501	0.105	0.121	0.117	0.046	0.146	0.030	n.p.
D	91-CW-9c	Ym	800	St-Grt(e)	0.443	0.010	-0.262	0.459	0.102	0.113	0.134	0.040	0.139	0.114	n.p.
D	93-CW-10	Ym	600	St-And-Grt(e)	0.410	0.009	0.285	0.480	0.097	n.a.	n.a.	n.a.	n.a.	n.a.	n.p.
D	93-CW-14a	Ym	370	St-Sil-And	0.438	0.014	0.291	n.a.	n.a.	n.p.	n.p.	n.p.	n.a.	n.a.	n.p.
D	91-Q-33	Ym	50	Sil-Grt(l)	0.484	0.009	-0.002	0.464	0.129	0.125	0.132	0.048	n.p.	n.p.	n.p.
D	93-CW-19a	Ym	50	Sil-Kfs-Grt(l)	0.482	0.025	0.093	n.a.	n.a.	n.a.	n.a.	n.a.	n.p.	n.p.	n.p.
	Average D				0.443	0.013	0.107	0.482	0.102	0.122	0.196	0.054	0.150	0.059	
E	92-A-3a	Ym	450	St-And-Grt(e)	0.457	0.008	0.040	0.494	0.089	0.108	0.165	0.054	0.133	0.113	n.p.
E	92-A-2c	Ym	300	St-And-Grt(e)	n.a.	n.a.	n.a.	0.462	0.090	0.096	0.104	0.057	0.151	n.a.	n.p.
F	92-ER-2c	Ym	250	And	0.473	0.010	-0.072	0.477	0.096	n.p.	n.p.	n.p.	n.p.	n.p.	n.p.
	Average E&F				0.465	0.009	-0.016	0.478	0.092	0.102	0.135	0.056	0.142		
G	92-SP-18a	Sl	500	Crd	0.494	0.005	0.167	0.552	0.085	n.p.	n.p.	n.p.	n.p.	n.p.	alt'd
G	92-SP-18b	Sl	500	Crd-And	0.483	0.004	0.197	0.526	0.075	n.p.	n.p.	n.p.	n.p.	n.p.	alt'd
G	92-SP-30c	Sl	80	Crd-Kfs	n.a.	n.a.	n.a.	0.537	0.105	n.p.	n.p.	n.p.	n.p.	n.p.	0.684
	Average G				0.489	0.004	0.182	0.538	0.088						
I	92-MH-5a	Sl	400	Crd-And	n.a.	n.a.	n.a.	0.418	0.067	n.p.	n.p.	n.p.	n.p.	n.p.	alt'd
I	92-MH-24	Sl	120	And	n.a.	n.a.	n.a.	0.384	0.165	n.p.	n.p.	n.p.	n.p.	n.p.	n.p.
	Average I							0.401	0.116						
J	93-NK-1	Sl	300	St-And-Sil	0.395	0.008	0.366	0.422	0.097	n.p.	n.p.	n.p.	0.151	0.046	n.p.
J	NB-52	Sl	350	St-And-Sil-Grt(e)	n.a.	n.a.	n.a.	0.408	0.090	0.100	0.108	0.034	0.124	n.a.	n.p.
	Average J							0.415	0.094				0.138		
K	92-FL-15a	Sl	750	And-St	0.443	0.006	0.023	0.450	0.074	n.p.	n.p.	n.p.	0.146	0.143	n.p.
K	92-FL-1b	Sl	0	Sil-Grt(l)	0.412	0.005	0.379	0.421	0.154	0.126	0.036	0.021	n.p.	n.p.	n.p.
	Average K				0.428	0.006	0.201	0.436	0.114						
All	Overall average				0.451	0.013	0.161	0.470	0.099	0.112	0.186	0.047	0.145	0.074	0.633

Column headings: SU: stratigraphic unit; Ym:Ymir Group, Sl: Slocan Group. Dist.: distance from contact, in m. All assemblages contain Ms + Bt + Qtz + Pl + Gr + Ilm ± Po + Tur ± Zrn ± Ap ± Mnz ± Xnt. Grt(e): early garnet; Grt(l): late garnet. WR1: Whole-rock Mg/(Mg + Fe), assuming that all the Fe is ferrous, and after removal of Fe associated with ilmenite and pyrrhotite (see text for further details). WR2: Whole-rock Mn/(Mn + Fe + Mg), with the same approach for Fe as in WR1. WR3: Whole-rock A value in AFM diagram (see text for details of projection scheme). Bt1: Matrix biotite Mg/(Mg + Fe), assuming that all Fe is ferrous. Bt2: Matrix biotite Ti, in number of cations per formula unit assuming 11 atoms of oxygen. Grt1: Garnet rim Mg/(Mg + Fe), assuming that all Fe is ferrous. Grt2: Garnet rim X_{Mn}, equal to Mn/(Mn + Ca + Fe + Mg). Grt3: Garnet rim X_{Ca}, equal to Ca/(Mn + Ca + Fe + Mg). St1: Staurolite rim Mg/(Mg + Fe), assuming that all Fe is ferrous. St2: Staurolite rim $X_{(Zn+Mn)}$ = (Zn + Mn) / (Zn + Mn + Fe + Mg). Crd: Cordierite rim Mg/(Mg + Fe), assuming that all Fe is ferrous. Abbreviations: n.a.: not analyzed, n.p.: mineral not present in the assemblage, alt'd: altered.

sentative sampling due to porphyroblast "nugget" effects, is an artifact of the projection scheme, or indicates meaningful differences in Al content is debatable and discussed below. Eighteen of the 24 bulk compositions have A values that fall on or below the garnet–chlorite tie-line. There is no significant difference in composition between the Ymir and Slocan metapelites (mean A value: 0.16 and 0.21, respectively; mean Mg/(Mg + Fe) value: 0.45 for both). The average whole-rock Mg/(Mg + Fe) at Nelson is very similar to that of average pelite worldwide (*e.g.*, Ague 1991).

PHASE EQUILIBRIA

Figure 3 shows schematically the low-pressure phase equilibria that pertain to the Nelson metapelitic assemblages. Reactions are listed in Table 2. The chemical system pertaining to Figure 3 and Table 2 is the model pelitic system K_2O–FeO–MgO–Al_2O_3–SiO_2–H_2O (KFMASH), a choice that is justified in more detail later in the paper. Reactions within this system account well for the significant modal changes observed in the rocks, recognizing that they are simplifications of the natural reactions that occur. One mineral that is not well modeled in KFMASH is garnet, which occurs as a modally minor, relatively unreactive phase in some of the rocks and is treated as an additional or "extra" phase stabilized by Mn and Ca. The stability field of garnet shown in Figure 3 therefore underrepresents its ocurrence in natural (Mn + Ca)-bearing rocks such as those in the

TABLE 2. MINERAL REACTIONS RELEVANT TO ASSEMBLAGES IN THE AUREOLE OF THE NELSON BATHOLITH, BRITISH COLUMBIA

	Fe- and Mg-free reactions	
1	And	= Sil
2	Ms + Qtz	= Als + Kfs + H_2O
17	Ms	= Crn + Kfs + H_2O
	Univariant reactions in KFMASH	
3	Ms + Chl + Grt + Qtz	= St + Bt + H_2O
4	Ms + Chl + St + Qtz	= Als + Bt + H_2O
5	Ms + Chl + Qtz	= Crd + And + Bt + H_2O
6	Ms + St + Qtz	= Grt + Als + Bt + H_2O
	Divariant reactions in KFMASH	
7	Ms + Chl + Qtz	= Grt + Bt + H_2O
8	St + Bt + Qtz	= Grt + Ms + H_2O
9	Ms + Grt	= Als + Bt + Qtz
10	Ms + Chl + Qtz	= St + Bt + H_2O
11	Ms + St + Qtz	= Als + Bt + H_2O
12	Ms + Chl + Qtz	= Als + Bt + H_2O
13	Ms + Chl + Qtz	= Crd + Bt + H_2O
14	Ms + Crd	= Als + Bt + Qtz + H_2O
15	Ms + Bt + Qtz	= Crd + Kfs + H_2O
16	Bt + Als + Qtz	= Crd + Kfs + H_2O

Als: Al_2SiO_5 mineral (andalusite or sillimanite).

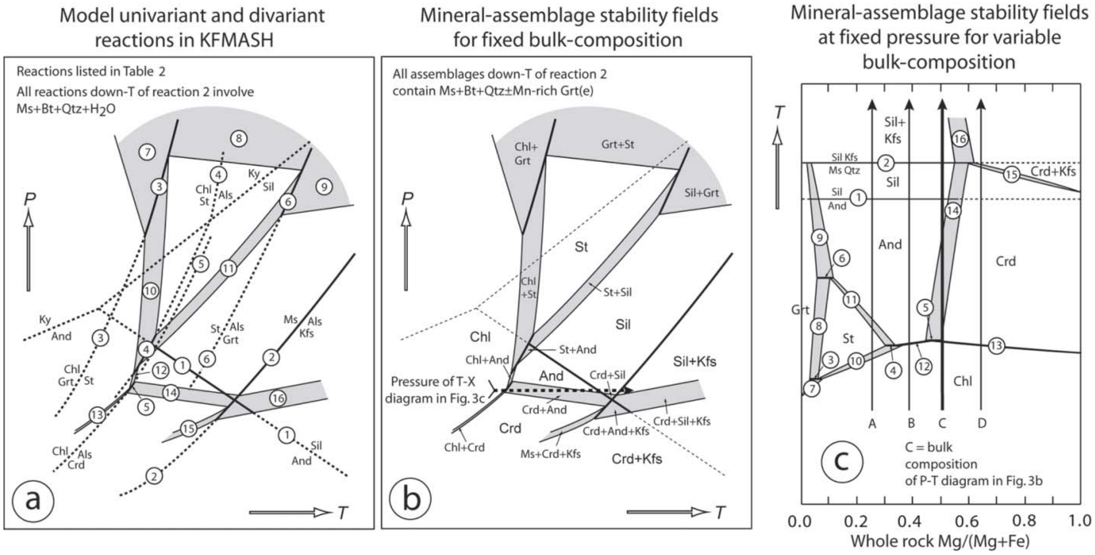

FIG. 3. Reactions and schematic representation of mineral-assemblage stabilities in the KFMASH system. Stability fields for mineral assemblages containing (Mn + Ca)-bearing garnet, such as found in the Nelson rocks, extend to lower pressure and temperature than shown in these diagrams (see Fig. 10). (a) Schematic P–T diagram showing numbered reactions discussed in the text and listed in Table 2. For clarity, only a portion of the full Fe–Mg divariant reaction intervals is shown. Dashed portions of reactions are not "seen" by the bulk composition of interest. (b) Schematic P–T diagram showing stability fields of mineral assemblages for a fixed bulk-composition. (c) Schematic isobaric T–$X_{Fe–Mg}$ diagram showing the dependence of mineral-assemblage stability on whole-rock Mg/(Mg + Fe).

Nelson aureole (see Distribution and Significance of Garnet below).

The qualitative topology of Figure 3 is based on the grids of Pattison & Tracy (1991) and Pattison *et al.* (1999, 2002), a choice that is justified later in the paper. Figure 3a is a schematic P–T diagram showing the location of the numbered reactions listed in Table 2, whereas Figure 3b is a schematic P–T diagram showing the distribution of stable assemblages of minerals in P–T space for a fixed bulk-composition. Figure 3c is a schematic isobaric T–X_{Fe-Mg} diagram that shows how different mineral assemblages can be developed at the same P–T conditions in rocks of differing bulk-rock Mg/(Mg + Fe).

Comparison of Figures 3b and 3c shows the two competing factors that influence the development of a given assemblage of minerals: bulk composition and P–T conditions. For bulk compositions of a fixed or restricted range of Mg/(Mg + Fe), (staurolite ± andalusite)-bearing assemblages are developed at a higher pressure than (cordierite ± andalusite)-bearing assemblages, with the two domains separated by a small interval in pressure in which andalusite-bearing assemblages develop without either staurolite or cordierite as coexisting or precursor phases (Fig. 3b). Figure 3c shows, in contrast, that (staurolite ± andalusite)-bearing assemblages can develop in Fe-rich compositions (*e.g.*, composition A) at the same P–T conditions that (cordierite + andalusite)-bearing and cordierite-only assemblages develop in Mg-rich compositions (*e.g.*, compositions C and D, respectively).

SEQUENCES OF MINERAL ASSEMBLAGES IN THE AUREOLE

The contact aureole of the Nelson Batholith was examined in twelve areas (labeled A–L in Fig. 1). Six of the areas (A–F) are located along the southern "tail" of the batholith within the Ymir Formation, whereas the remaining six (G–L) are located along the northern and eastern margins of the main batholith within the Slocan Group. The contact aureole of the Bonnington Pluton also was examined (area M in Fig. 1). Particular emphasis is placed on areas A, B and D because they are adjacent to each other along the southern tail of the batholith and show a progressive change in prograde sequence of mineral assemblages.

Maps showing the distribution of mineral assemblages from areas A–F and G–K are shown in Figures 4a and 4b, respectively. Mineral abbreviations are from Kretz (1983). All assemblages in the aureole, and >90% of those outside of the aureole, contain biotite, reflecting the pre-intrusion biotite-grade regional metamorphism. All assemblages contain quartz, muscovite, plagioclase and graphite, in addition to some or all of ilmenite, tourmaline, zircon, monazite, pyrrhotite, xenotime, and allanite. Chlorite and fine-grained white mica ("sericite") are commonly present as secondary minerals. Photomicrographs are provided in Figures 5 and 6.

Minerals from 23 samples were analyzed with wavelength dispersion on either an ARL SEMQ electron microprobe or JEOL JXA–8200 electron microprobe, both at the University of Calgary, using standard operating conditions (15 kV, 20 nA, focused beam) and a range of well-characterized natural and synthetic standards (*e.g.*, Nicholls & Stout 1988). Results from five samples analyzed on both instruments are in excellent agreement. Representative compositions for biotite, muscovite, garnet, staurolite, cordierite, and plagioclase are provided in Appendices 2–7, respectively, and a summary of key compositional parameters of the minerals is provided in Table 1. Figure 7 shows whole-rock compositions and mineral compositions plotted in AFM diagrams for each area. In Figure 2a, biotite compositions are plotted along with the whole-rock compositions discussed above. The mean and range of Mg/(Mg + Fe) in biotite is similar to that of the whole-rock compositions.

Mineral reactions are discussed according to the numbering scheme in Table 2 and Figure 3. Figure 8a is a qualitative P–T diagram, corresponding to the low-pressure part of Figure 3b, on which the sequences of mineral assemblages from the different areas are plotted. For simplicity, the P–T paths are assumed to be isobaric.

Area A: the southernmost part of the tail (*Fig. 4a*)

The width of the aureole in area A, based on the outermost occurrence of porphyroblasts of cordierite, is about 700 m. Crd + Bt is the dominant assemblage, with the exception of two samples from within 50 m of the intrusive contact that contain pseudomorphs after andalusite in addition to cordierite. Cordierite occurs as ovoid porphyroblasts with diffuse margins that have overgrown the regional foliation (Fig. 5a). Cordierite in most samples is completely altered to fine-grained chlorite and "sericite", with the exception of some samples near 92–PC–19A (Fig. 4a). Pseudomorphs after andalusite have a more rectilinear outline and typically contain coarser grained material that is richer in "sericite". Garnet occurs in a single Crd + And + Bt sample adjacent to the contact (92–PC–27b) as euhedral, largely altered grains <200 μm in diameter, within the matrix and in some cases as inclusions in cordierite. The garnet is interpreted to be of early-stage origin, predating growth of cordierite and andalusite, and is termed Grt(e).

The occurrence of Crd + Bt assemblages upgrade of cordierite-free, chlorite-bearing rocks suggests that cordierite was produced from the KFMASH divariant reaction:

$$\text{Ms} + \text{Chl} + \text{Qtz} = \text{Crd} + \text{Bt} + H_2O. \quad (13)$$

The abundance of chlorite-free Crd + Bt assemblages suggests that in most rocks, chlorite was consumed by reaction 13. The rare development of And + Crd + Bt at high grade suggests progress of the KFMASH divariant reaction:

$$\mathrm{Ms + Crd = And + Bt + Qtz + H_2O}, \qquad (14)$$

or, where the bulk composition is more Fe-rich, by the KFMASH univariant reaction:

$$\mathrm{Ms + Chl + Qtz = And + Crd + Bt + H_2O}, \qquad (5)$$

in which case both andalusite and cordierite were produced by chlorite breakdown and persisted upgrade (see Fig. 3c). An isobaric metamorphic field-gradient that satisfies the sequence of reactions for area A is shown in Figure 8a.

Area B: the southern part of the tail (*Fig. 4a*)

The width of the aureole in area B, based on the outermost occurrence of porphyroblasts of andalusite, is about 700 m. Andalusite porphyroblasts appear upgrade of Chl + Bt phyllites, giving rise to abundant assemblages of And + Bt that occurs up to the sillimanite isograd. A single sample on the isograd contains the assemblage And + Chl + Bt. The andalusite porphyroblasts are 0.5–5 mm long and typically show a chiastolitic pattern of inclusions or accumulations of graphite and opaque phases along rectilinear grain-edges, or both (Figs. 5b, c). Andalusite may be partly or wholly altered to fine- to coarse-grained "sericite". A single sample containing Crd + Bt was collected from the And + Bt zone in the north part of area B (92–OC–15a in Fig. 4a), reflecting a more magnesian bulk-composition (Table 1, Fig. 7b).

The onset of the sillimanite zone, *ca.* 450 m from the contact, is marked by the appearance of fibrolitic and fine-grained sillimanite (for a distinction, see Pattison 1992). The sillimanite occurs in mats within the matrix and in fine needles intergrown with biotite or muscovite. At higher grade within the sillimanite zone, *ca.* 200 m from the contact, sillimanite directly replaces andalusite (Fig. 5d). Within 50 m of the contact, K-feldspar occurs in muscovite-poor, sillimanite-rich samples containing a few relict crystals of andalusite largely replaced by coarse sillimanite. The K-feldspar occurs in anhedral, cryptoperthitic crystals associated with quartz and variable amounts of sillimanite, in discrete granular domains of a coarser grain-size than the matrix. This texture resembles the occurrence of K-feldspar in areas D and I (Figs. 5g, 6g), and may be indicative of incipient fusion (partial melting).

Manganese-rich garnet (<1% modally) has been observed in two low-grade argillites immediately downgrade of the andalusite isograd and in three samples from the sillimanite zone (Fig. 4a). In all cases, it occurs as small euhedral crystals (<200 μm diameter) scattered evenly throughout the rock. In the And + Sil + Bt rocks, euhedral crystals of garnet occur as inclusions in andalusite with the same grain-size and habit as those in the matrix (Fig. 5c), suggesting that it was not involved significantly in the modal changes associated with the development of andalusite and sillimanite. As in area A, this garnet is inferred to predate the development of andalusite and is termed Grt(e).

The occurrence of And + Bt ± Chl assemblages upgrade of andalusite-free, chlorite-bearing rocks (Fig. 4a) suggests that andalusite was produced from the KFMASH divariant reaction:

$$\mathrm{Ms + Chl + Qtz = And + Bt + H_2O}. \qquad (12)$$

The development of sillimanite upgrade of the And + Bt suggests the reaction:

$$\mathrm{And = Sil}. \qquad (1)$$

The development of K-feldspar and marked reduction in muscovite at the highest grade indicate progress of the reaction:

$$\mathrm{Ms + Qtz = Sil + Kfs + H_2O \text{ or } L}. \qquad (2)$$

(where L represents silicate liquid). Because K-feldspar and textural evidence for melting are both present in sample 03–OC–2b, and neither is present in the next lowest grade sample (Fig. 4a), we are unable to conclude whether melting preceded K-feldspar growth or *vice versa*.

An isobaric metamorphic field-gradient that satisfies the above sequence of reactions for area B, including the near-coincidence of reaction 2 with the onset of melting, is shown in Figure 8a. The predominance of cordierite-free And + Bt assemblages in rocks of similar bulk-composition to area A indicates that area B lies at a higher pressure than area A.

Area C: the south-central part of the tail (*Fig. 4a*)

Because only a few samples could be obtained from area C, it is not considered in detail. Area C is significant, however, in being the first area to the north of areas A and B to develop staurolite. The width of the aureole, based on the outermost occurrence of porphyroblasts of staurolite, is about 1000 m. The dominant assemblage upgrade of the regional Chl + Bt argillites is St + Bt + Grt(e), occurring in rocks with a similar grain-size and texture to the staurolite-bearing assemblages from area D, to be discussed in detail below. There is a lack of higher grade (*e.g.*, Al_2SiO_5-bearing) mineral assemblages in area C, even within 300 m of the contact. The occurrence of St + Bt assemblages suggests that area C is at higher pressure than area B (Fig. 8a).

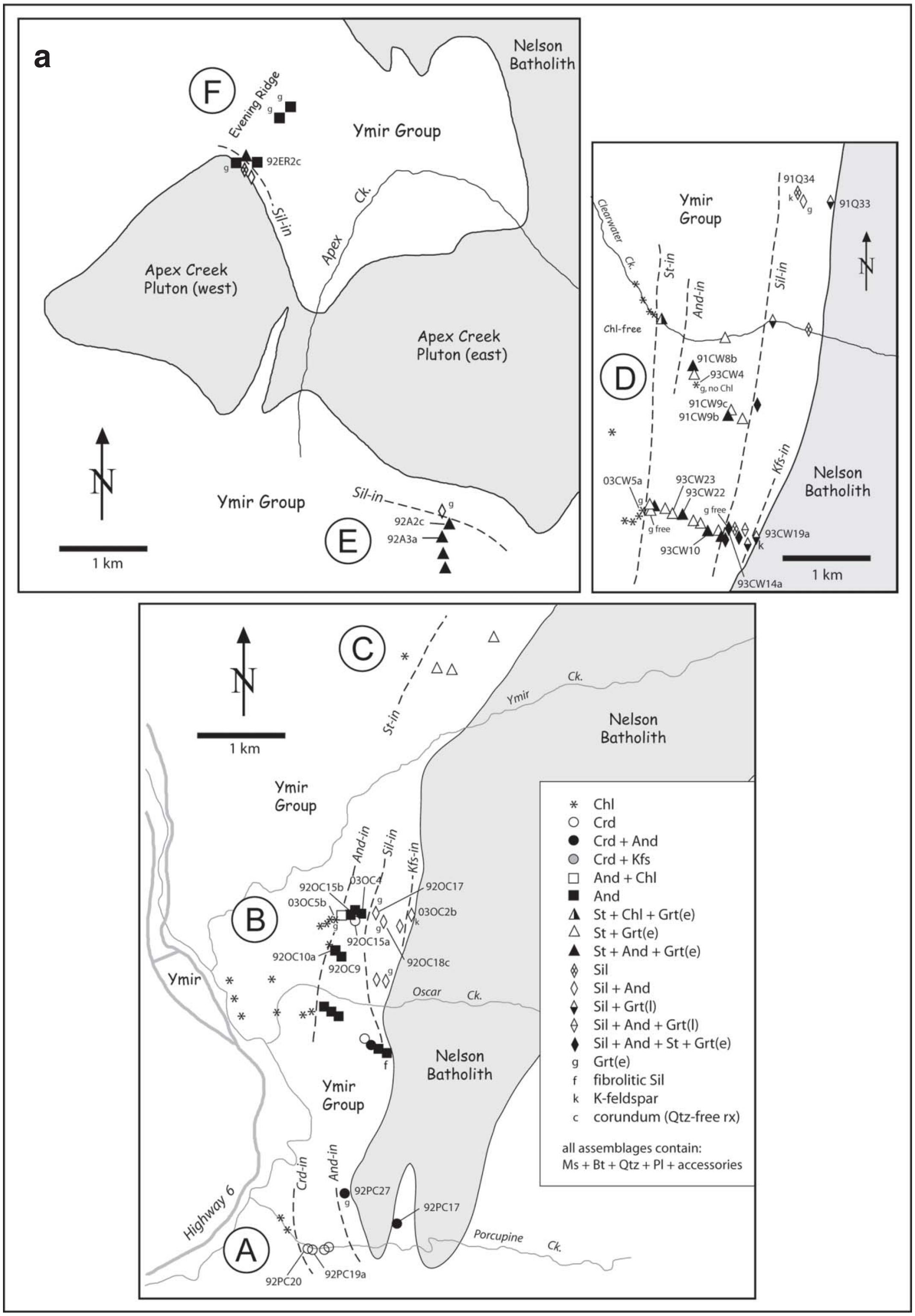
a
F
Evening Ridge
92ER2c
Sil-in
Ymir Group
Nelson Batholith
Apex Ck.
Apex Creek Pluton (west)
Apex Creek Pluton (east)
Ymir Group
Sil-in
92A2c
92A3a
E
1 km
N
D
Ymir Group
Clearwater Ck.
St-in
And-in
Sil-in
Kfs-in
91Q34
91Q33
Chl-free
91CW8b
93CW4
g, no Chl
91CW9c
91CW9b
03CW5a
93CW23
93CW22
g free
93CW10
93CW19a
93CW14a
Nelson Batholith
1 km
C
St-in
Ymir Ck.
Nelson Batholith
1 km
Ymir Group
B
And-in
Sil-in
Kfs-in
92OC15b
03OC4
03OC5b
92OC17
03OC2b
92OC15a
92OC10a
92OC9
92OC18c
Ymir
Oscar Ck.
Ymir Group
Nelson Batholith
Highway 6
Crd-in
And-in
92PC27
92PC17
A
92PC20
92PC19a
Porcupine Ck.
* Chl
○ Crd
● Crd + And
● Crd + Kfs
□ And + Chl
■ And
▲ St + Chl + Grt(e)
△ St + Grt(e)
▲ St + And + Grt(e)
◇ Sil
◇ Sil + And
◆ Sil + Grt(l)
◇ Sil + And + Grt(l)
◆ Sil + And + St + Grt(e)
g Grt(e)
f fibrolitic Sil
k K-feldspar
c corundum (Qtz-free rx)
all assemblages contain:
Ms + Bt + Qtz + Pl + accessories

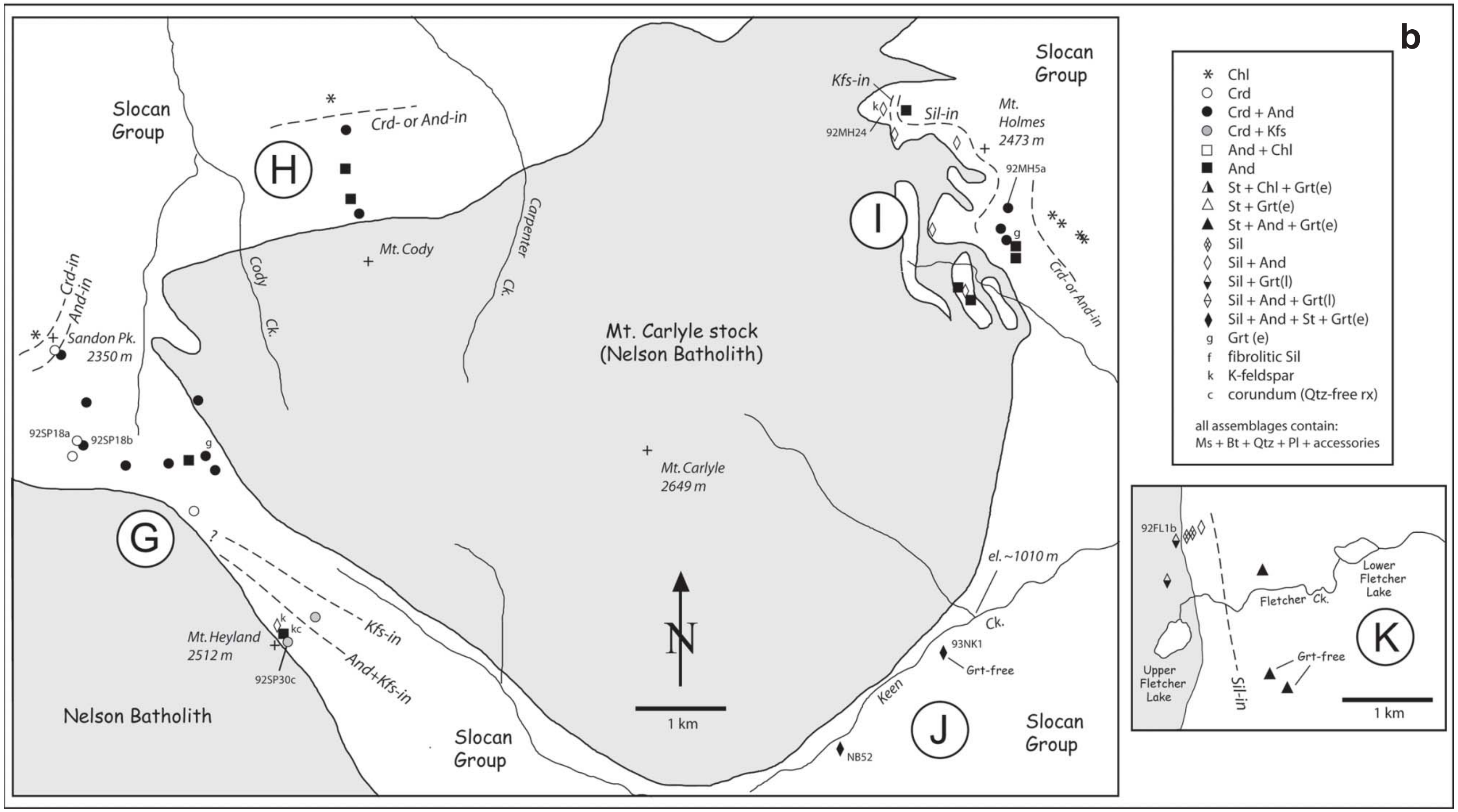

FIG. 4. Mineral assemblages, isograds and analyzed samples from areas A – K (see Fig. 1 for location of areas). In sillimanite-bearing samples, andalusite and staurolite are interpreted to be unstable relics. Grt(e): early-formed garnet, Grt(l): late garnet. (a) Maps of areas A–F. (b) Maps of areas G–K.

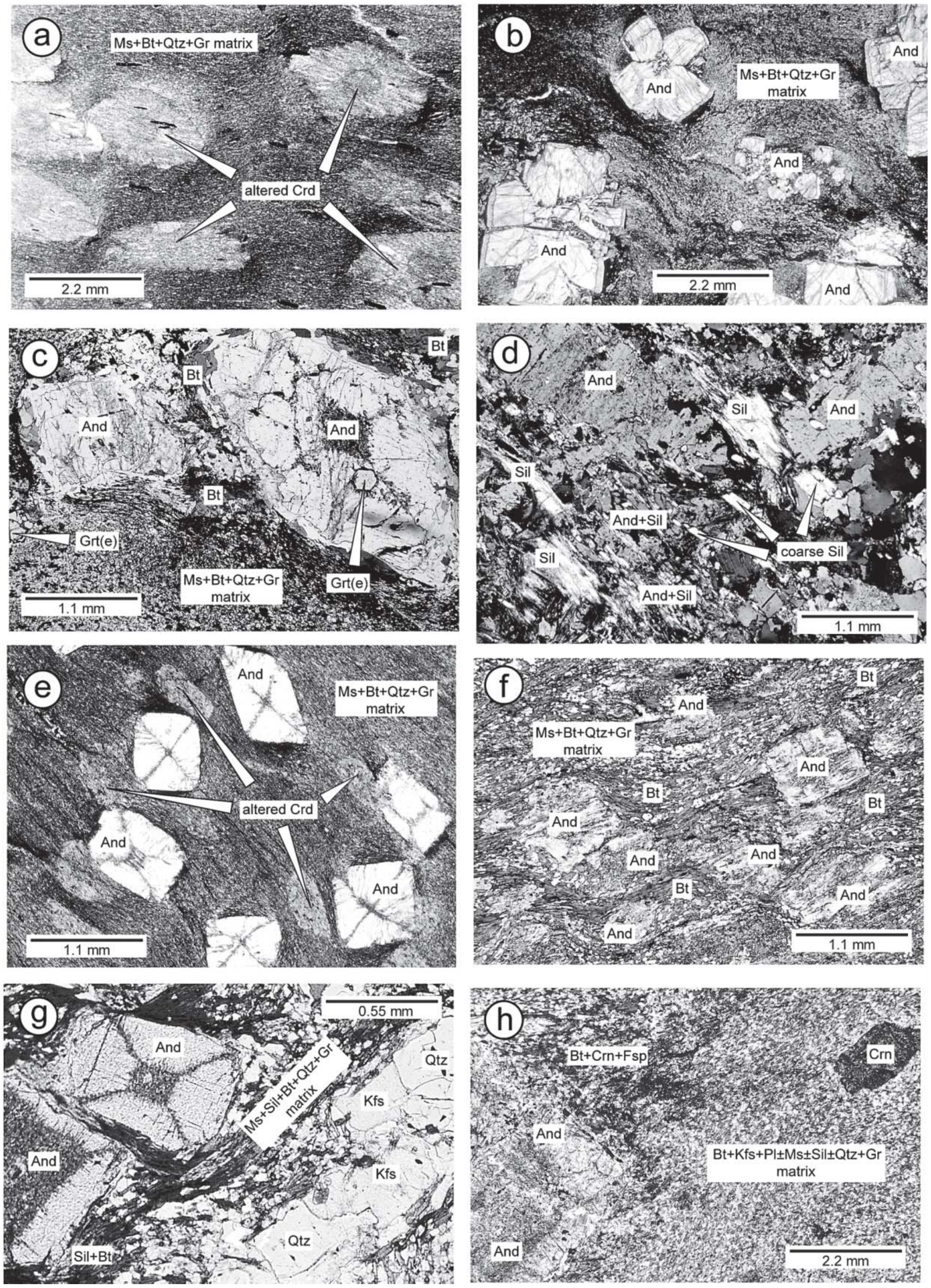

FIG. 5. Photomicrographs of lower-pressure mineral assemblages from the cordierite ± andalusite and andalusite-only domains of the Nelson aureole (Figs. 4, 9). (a) Altered cordierite porphyroblasts in a fine-grained graphitic matrix, sample 92–PC–20, area A. (b) Andalusite porphyroblasts in a fine-grained graphitic matrix, 92–OC–10a, area B. (c) Early garnet, Grt(e), included within andalusite, 92–OC–18c, area B. (d) Fine- and coarse-grained sillimanite intergrown with and replacing andalusite, upgrade of 92–OC–18c, area B. (e) Altered cordierite and fresh andalusite porphyroblasts in a fine-grained graphitic matrix, sample 92–MH–5a, area I. (f) Andalusite porphyroblasts in a foliated, biotite-rich matrix, area H. (g) Andalusite crystals and a coarse-grained segregation of K-feldspar and quartz in a (Ms + Sil)-bearing matrix. Sample 92–MH–24, area I. (h) Corundum and andalusite in a sillimanite-bearing matrix, near sample 92–SP–30c, area G.

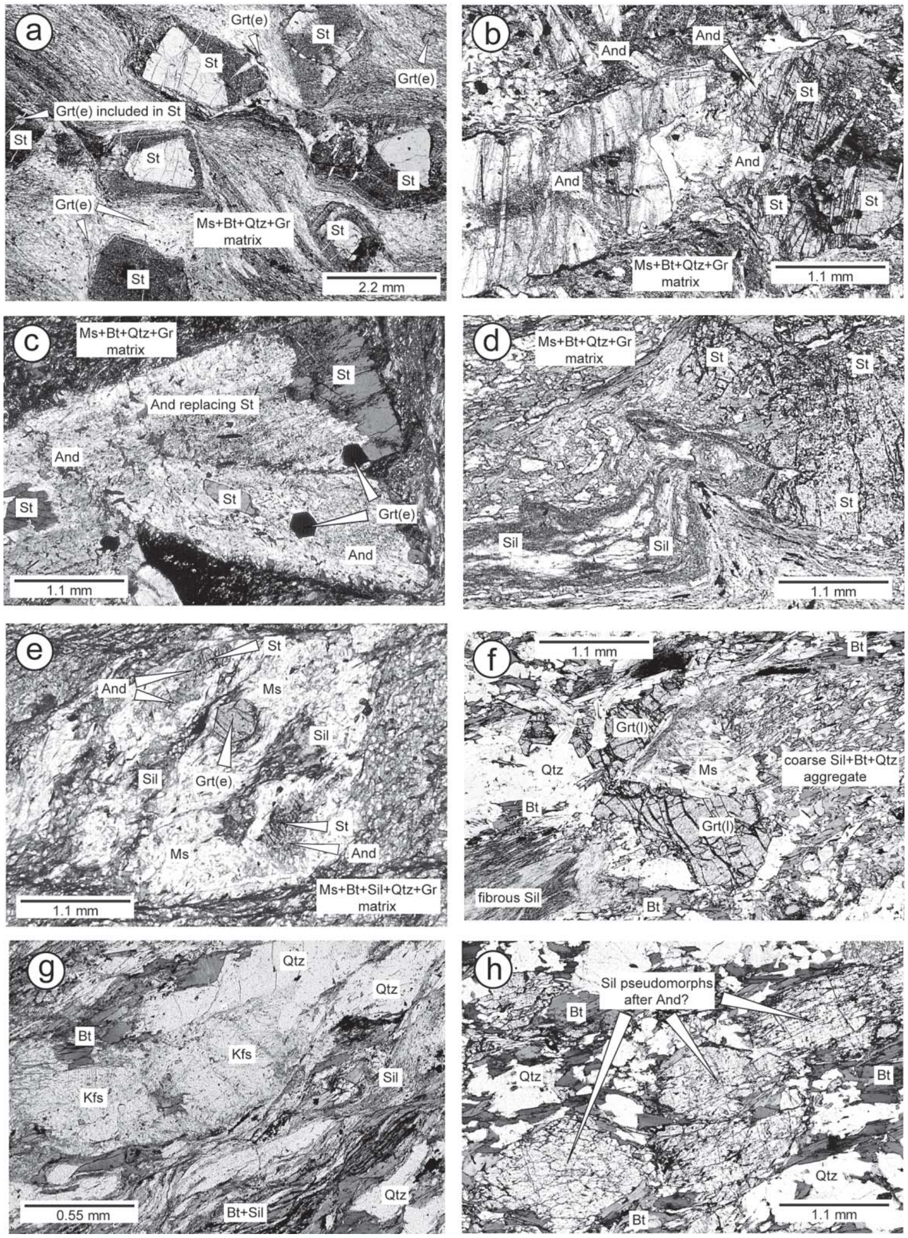

FIG. 6. Photomicrographs of higher-pressure mineral assemblages from the staurolite ± andalusite domain of the Nelson aureole (Figs. 4, 9). (a) Staurolite porphyroblasts in a fine-grained graphitic matrix, sample 91–CW–9b, area D. Early-formed garnet, Grt(e), occurs as euhedral crystals in the matrix and as euhedral inclusions in staurolite. (b) Andalusite and staurolite, sample 91–CW–9c, area D. (c) Partial replacement of staurolite by andalusite, sample 93–CW–10, area D. Euhedral inclusions of early garnet, Grt(e), are of a similar size and shape to those at lower grade. (d) Staurolite and sillimanite, upgrade of sample 93–CW–10, area D. (e) Coarse-grained muscovite pseudomorph after staurolite (?), upgrade of sample 93–CW–10, area D. The coarse-grained muscovite contains sillimanite and remnants of andalusite and staurolite, in addition to a euhedral inclusion of early-formed garnet, Grt(e). (f) Fibrous matrix sillimanite and coarser-grained aggregates of sillimanite, biotite and quartz, sample 91–Q–33, area D. Late garnet, Grt(l), is of a different grain-size and texture compared to the Grt(e) seen at lower grade. (g) Segregation of relatively coarse-grained K-feldspar and quartz in a (Bt + Sil)-bearing matrix, sample 93–CW–19a, area D. (h) Coarse-grained sillimanite, possibly a pseudomorph of andalusite, in a biotite-bearing matrix, east of sample 92–FL–1b, area K.

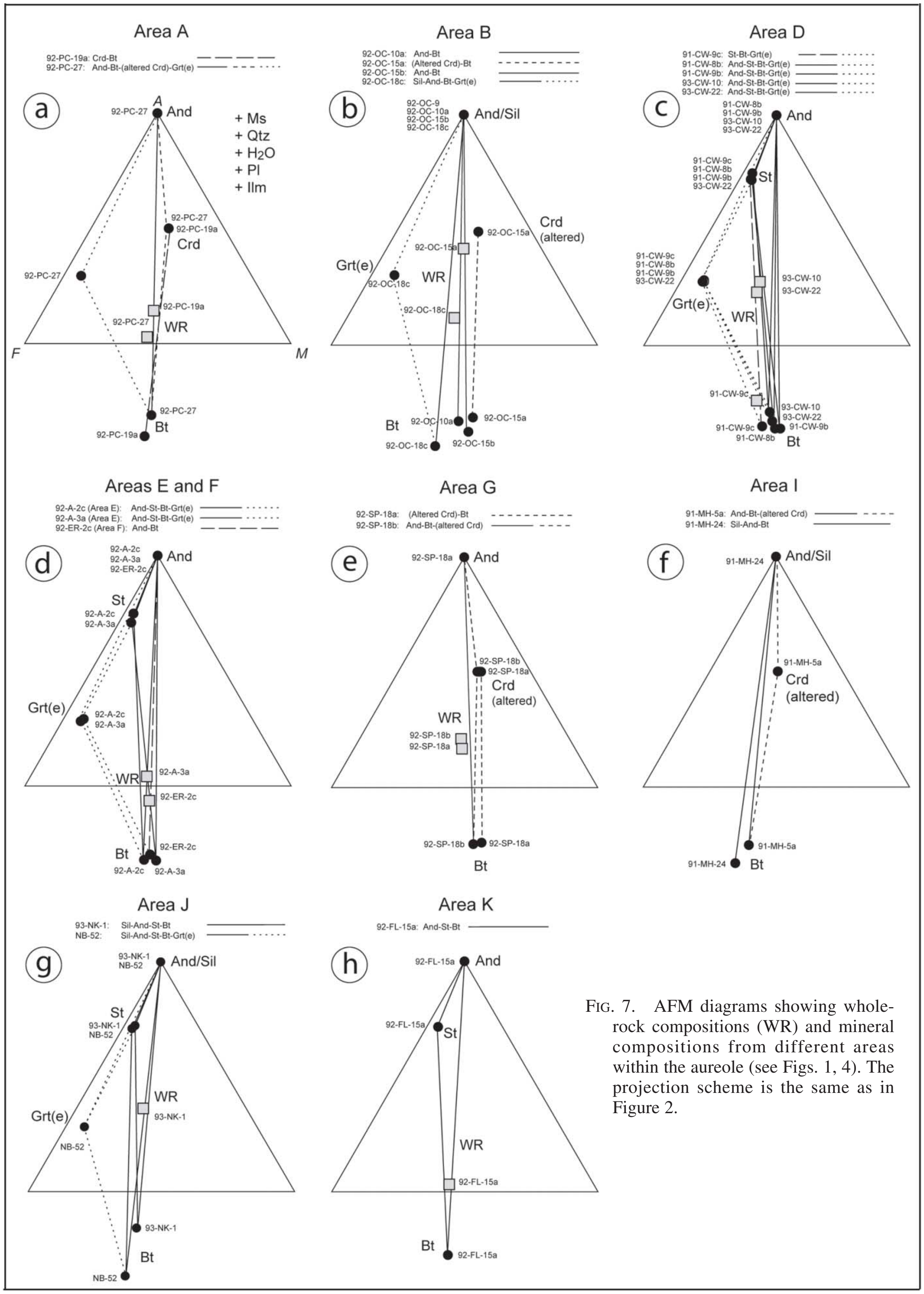

FIG. 7. AFM diagrams showing whole-rock compositions (WR) and mineral compositions from different areas within the aureole (see Figs. 1, 4). The projection scheme is the same as in Figure 2.

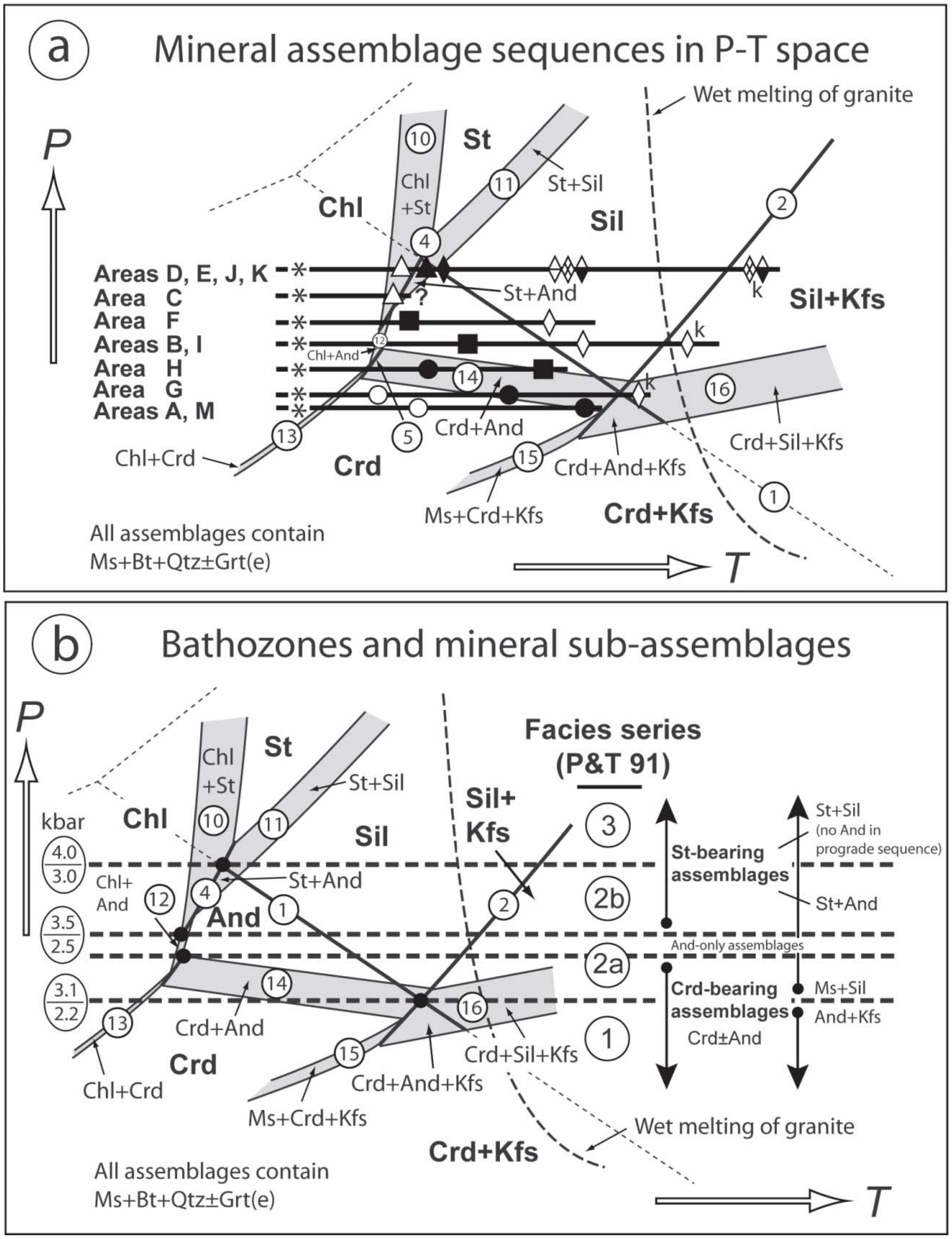

FIG. 8. (a) Rationalization of mineral-assemblage sequences in the Nelson aureole in P–T space. Mineral-assemblage symbols are the same as in Figure 4. Reaction numbering is provided in Table 2. The positioning of the isobaric lines is representative and takes account of the most common assemblages of minerals in each area. Not every area spans the full range of grade (for example, areas E, J and K do not go to a sufficiently high grade to develop K-feldspar, but their mineral assemblages at lower grade are similar to those in area D). (b) Division of P–T space into bathozones defined by key subassemblages, corresponding to the mineral-assemblage domains in Figure 9. Absolute pressures of the bathograds that separate the bathozones are shown in the ovals. The higher set of pressures is based on Figure 11a and is tied to the Pattison (1992) Al_2SiO_5 triple point, whereas the lower set of pressures is based on Figure 10d of Pattison *et al.* (2002) and is tied to the Holdaway (1971) Al_2SiO_5 triple point. Numbered reactions are given in Table 2.

Area D: the central part of the tail (*Fig. 4a*)

The width of the aureole in area D, based on the outermost occurrence of porphyroblasts of staurolite, varies from 1300 m in the southern part of the area to 1800 m in the northern part of the area (Fig. 4a). The distances listed below are made with reference to the main suite of samples in the southern part of the area.

Staurolite porphyroblasts appear upgrade of Chl + Bt±Grt(e) argillites. A single sample contains St + Bt + Chl + Grt(e). Chlorite-free St + Bt + Grt(e) assemblages persist upgrade to and beyond the andalusite isograd. Prismatic staurolite is 1–5 mm in size and varies from poikiloblastic to relatively inclusion-free, in some cases showing twinning and sector zoning (Fig. 6a).

Garnet is a common accessory phase in these assemblages. It typically occurs as small (<500 μm), euhedral to subhedral crystals scattered throughout the rock and in some cases as inclusions in staurolite that have the same grain-size and habit as garnet crystals in the matrix (Figs. 6a, c, e). This garnet is termed Grt(e) in keeping with that in areas A and B. Grt(e) predates staurolite growth and texturally appears to have behaved more or less as a passive phase that was not involved significantly in the development of staurolite (*e.g.*, little evidence for dissolution: Figs. 6a, c). A contact-metamorphic garnet zone, predicted to occur downgrade of the staurolite-in isograd, is narrow to non-existent on the basis of the samples collected (Fig. 4a), suggesting that the conditions of formation of Grt(e) were not very different than those for staurolite. Grt(e) has been identified upgrade to the sillimanite zone, through which interval it shows the same textural relations, as noted above.

About 900 m from the intrusive contact, andalusite appears in the assemblage And + St + Bt + Grt(e) as highly anhedral poikiloblasts. At higher grade, andalusite occurs as discrete, commonly chiastolitic porphyroblasts (Fig. 6b) and as partial pseudomorphs and rims on staurolite porphyroblasts (Figs. 6b, c), with both varieties occurring in some rocks. Andalusite-free St + Bt + Grt(e) assemblages also occur within the andalusite zone and may occur in the same outcrop and even in the same thin section as andalusite-bearing assemblages.

The sillimanite isograd occurs 400 m from the intrusive contact and is marked by fine-grained sillimanite growing in the matrix and on the margins of andalusite and staurolite porphyroblasts (Fig. 6d). Three hundred meters from the contact, the rocks take on a more schistose, less porphyroblastic appearance. Andalusite porphyroblasts, in some cases with ragged inclusions of staurolite, are partially to wholly replaced by coarse muscovite (Fig. 6e). Sillimanite is abundant in the coarse muscovite and in the matrix. In some rocks, aggregates of prismatic sillimanite are intergrown with biotite and quartz (Fig. 6f), possibly representing pseudomorphs after staurolite. The last occurrence of staurolite is about 100 m from the contact, but a staurolite-out isograd has not been mapped on this basis because of the evidence that staurolite is an unstable relic at this grade (Figs. 6c, e).

A second textural variety of garnet appears in some rocks upgrade of the last occurrence of staurolite, characterized by 3–5 mm, xenoblastic crystals intergrown with biotite and quartz (Fig. 6f). This latter variety of garnet is termed Grt(l). Whether Grt(l) represents a newly formed variety of garnet produced during staurolite consumption, or indicates recrystallization of earlier formed Grt(e), is uncertain.

Within 100 m of the contact, K-feldspar occurs in the assemblage Ms + Qtz + Kfs + Sil + Bt ± Grt, marking the K-feldspar isograd. K-feldspar occurs in medium- to coarse-grained segregations of anhedral, variably perthitic crystals intergrown with quartz and sillimanite (Fig. 6g), suggestive of leucosome development by partial melting. By contrast, an isolated occurrence of Sil + Kfs (91–Q–34) was found 300 m from the contact in the northern part of area D, interbedded with rocks containing And + St (Fig. 4a). The K-feldspar in this sample occurs as discrete, ovoid, 3–7 mm, inclusion-filled porphyroblasts in the matrix, with no evidence for leucosome development.

The occurrence of St + Bt + Grt(e) assemblages upgrade of Chl + Bt ± Grt(e) argillites, combined with the lack of evidence for significant participation of Grt(e) in the formation of staurolite, suggests that staurolite was produced by the KFMASH divariant reaction:

$$\text{Ms} + \text{Chl} + \text{Qtz} = \text{St} + \text{Bt} + \text{H}_2\text{O}. \qquad (10)$$

Chlorite is interpreted to have been consumed in most rocks by reaction 10. The development of andalusite at the expense of staurolite in the assemblage And + St + Bt + Grt(e) is inferred to have occurred by the KFMASH divariant reaction:

$$\text{Ms} + \text{St} + \text{Qtz} = \text{And} + \text{Bt} + \text{H}_2\text{O}, \qquad (11)$$

or, if chlorite was not entirely consumed in reaction 10, by the KFMASH univariant reaction:

$$\text{Ms} + \text{St} + \text{Chl} + \text{Qtz} = \text{And} + \text{Bt} + \text{H}_2\text{O}. \qquad (4)$$

Reactions 4 and 11 mark the onset of the demise of staurolite. The occurrence of andalusite-free, staurolite-bearing assemblages hundreds of meters upgrade of where staurolite first starts to break down to andalusite, in rocks of similar whole-rock and mineral compositions (Table 1), points to sluggish kinetics of staurolite breakdown.

Addition of sillimanite to the And + St + Bt + Grt(e) assemblage suggests the reaction:

$$\text{And} = \text{Sil}. \qquad (1)$$

The development of K-feldspar suggests the progress of:

$$\text{Ms} + \text{Qtz} = \text{Sil} + \text{Kfs} + \text{H}_2\text{O or L}. \quad (2)$$

The textural evidence for melting suggests that reaction 2 involved liquid and therefore occurred above the solidus. The isolated occurrence of Kfs + Sil 300 m from the contact (91–Q–34) suggests the localized progress of reaction 2 below the solidus, perhaps owing to reduced activity of H_2O.

A metamorphic field-gradient that satisfies the above sequence of reactions is shown in Figure 8a. This path is interpreted to lie at higher pressure than area B because of the abundance of St ± And assemblages. Area C, which also contains abundant staurolite-bearing assemblages, is interpreted to be at lower pressure than area D and at higher pressure than area B because it occurs between areas B and D (Fig. 1).

Areas E and F: Apex Creek plutons, northwestern part of the tail (*Fig. 4a*)

Area E is dominated by assemblages similar to those in the St–And zone of area D, namely And + St + Bt + Grt(e). A single staurolite-free And + Sil + Bt + Grt(e) sample was collected from this transect. Compared to area D, the staurolite crystals are finer grained (<1 mm) and more euhedral, and the andalusite crystals are more anhedral and poikiloblastic. Area F is dominated by assemblages similar to those in the andalusite and sillimanite zones of area B, namely And + Bt ± Grt(e) at intermediate grade and Sil + Bt ± And ± Grt(e) at higher grade. A single sample contains <1% staurolite in addition.

Figure 8a shows metamorphic field-gradients for areas E and F. The sequence of mineral assemblages for area E is indistinguishable from that for area D. That for area F resembles that for area B, but has been placed at a slightly higher pressure because of the local development of staurolite and the more widespread occurrence of Grt(e), both indicative of higher-pressure conditions (more discussion below).

Area G: north-central main batholith (*Fig. 4b*)

Area G is located adjacent to the north-central contact of the Nelson Batholith, in an area where a septum of country rocks 1–2 km wide lies between the main mass of the batholith and the Mt. Carlyle Stock (Figs. 1, 4b). The width of aureole in area G, based on the outermost occurrence of porphyroblasts of cordierite, is about 1500 m.

Cordierite appears upgrade of Chl + Bt phyllites, giving rise to the assemblage Crd + Bt ± Chl in which cordierite overprints the foliation. About 100 m upgrade of the first appearance of cordierite, the andalusite isograd is encountered, marked by the development of Crd + And + Bt assemblages. These assemblages occur in much of the septum, along with Crd + Bt assemblages and a single And + Bt assemblage (Fig. 5f). Andalusite and cordierite porphyroblasts, the latter invariably altered (Fig. 5e), are typically wrapped by a weak to moderate foliation subparallel to the intrusive contact, indicating post-metamorphic deformation most likely related to the latter stages of emplacement of the composite batholith. A single And + Crd + Bt sample contains Grt(e).

The highest-grade rocks in area G are adjacent to the contact of the main batholith in the central part of the septum. Assemblages of Ms + Crd + Kfs + Bt occur within 450 m of the contact, allowing delineation of a K-feldspar isograd. Within 100 m of the contact, (Ms + And + Kfs)-bearing assemblages occur upgrade of an inferred And + Kfs isograd. In addition, sparse fibrolitic sillimanite occurs in these rocks. K-feldspar in these samples occurs in the matrix or spatially associated with andalusite (or both), rather than in (Kfs + Qtz)-rich segregations like those observed in areas B and D, suggesting that And + Kfs developed in area G under subsolidus conditions. In some quartz-free rocks at this grade, corundum also occurs (Fig. 5h), the latter commonly with a halo of K-feldspar.

The development of Crd + Bt assemblages upgrade of (Chl + Bt)-bearing regional argillites is ascribed to reaction 13. The development of And + Crd + Bt assemblages is ascribed to either reaction 14 or reaction 5, the latter reaction favored in more Fe-rich bulk compositions (Fig. 3c). The distinctive low-pressure Ms + Crd + Kfs + Bt assemblage is ascribed to progress of the KFMASH divariant reaction:

$$\text{Ms} + \text{Bt} + \text{Qtz} = \text{Crd} + \text{Kfs} + \text{H}_2\text{O} \quad (15)$$

in a magnesian bulk-composition, which, at lower grade, contained Ms + Crd + Bt without andalusite (Fig. 3c). Assemblages of And + Kfs containing sparse fibrolitic sillimanite but no evidence for partial melting suggest progress of reaction 2 at conditions below the solidus and near, but probably slightly below, the intersection of reaction 2 with reaction 1. The occurrence of Crn + Kfs indicates progress of the quartz-free reaction:

$$\text{Ms} = \text{Crn} + \text{Kfs} + \text{H}_2\text{O}. \quad (17)$$

The mineral assemblages in area G reflect a wider range of bulk composition than in other areas, making it difficult to plot a single isobaric metamorphic field-gradient that satisfies all the assemblages. Focusing on the abundance of Crd + And assemblages, area G is inferred to occur at a pressure between those of areas A and B, near the intersection of reactions 1 and 2 (Fig. 8a).

Area H: northwestern Mt. Carlyle Stock (*Fig. 4b*)

The width of the aureole in area H, as defined by the outermost occurrence of cordierite or andalusite, is 1200

m. Although the range of assemblages is similar to that in area G, including a And + Crd + Bt zone of substantial width, the rocks do not reach as high a grade (no K-feldspar-bearing assemblages observed), there is a greater proportion of cordierite-free And + Bt assemblages, and no Crd + Bt assemblages were found. Assuming the same average bulk-composition, the metamorphic field-gradient for area H in Figure 8a is therefore placed between those for areas B and G.

Area I: northeastern Mt. Carlyle Stock (*Fig. 4b*)

The width of the aureole in area I, based on the outermost occurrence of porphyroblasts of andalusite, is about 800 m. Assemblages in the porphyroblastic zone are dominated by And + Bt (Fig. 5f) and, at higher grade, within *ca.* 200 m of the contact, by Sil + And + Bt. Assemblages with And + Crd + Bt (Fig. 5e) are restricted to one small area south of Mt. Holmes. A single sample adjacent to the contact contains the Ms-absent assemblage Sil + And + Kfs (Fig. 5g). K-feldspar in this sample occurs as anhedral crystals in Kfs + Qtz segregations that are coaser grained than the matrix, as observed in areas B and D (Fig. 6g), and therefore suggestive of leucosome development by partial melting.

The development of abundant And + Bt assemblages upgrade of (Chl + Bt)-bearing regional argillites is ascribed to reaction 12, with the restricted And + Crd + Bt assemblages ascribed to the progress of reaction 5, perhaps preceded by reactions 12 or 13, in a more magnesian bulk-composition (Fig. 3c). The development of sillimanite is ascribed to reaction 1, and the development of Kfs + Sil upgrade of the first development of sillimanite, to reaction 2. Area I shows the same range of features as area B, and is therefore grouped with area B in Figure 8a.

Area J: southeastern Mt. Carlyle Stock (*Fig. 4b*)

Two samples were collected *ca.* 350 m from the southeastern margin of the Mt. Carlyle Stock, where a septum of country rocks *ca.* 3 km wide occurs between it and the main Nelson Batholith (Figs. 1, 4b). Both samples contain the assemblage And + Sil + St + Bt, with one containing in addition a small amount of Grt(e). An insufficient number of samples was collected to constrain the width of the aureole in this area. The similarity of the mineral assemblages and mineral compositions to those of areas D and F (Fig. 7) suggests that the pressure of area J also is similar (Fig. 8a).

Area K: northeastern main batholith (*Fig. 4b*)

In area K, the metapelites are not as rich in graphite as those from the other areas. Rocks farthest from the contact contain the assemblage St + And + Bt without Grt(e). Staurolite porphyroblasts are commonly small (<1 mm long), euhedral, and constitute less than 2% of the rock. Andalusite is poikiloblastic. One St + And + Bt sample in this zone also contains small euhedral grains of Grt(e). The sillimanite isograd is poorly constrained to between 250 and 600 m from the contact. Within 150 m of the contact, two samples contain grains of coarse sillimanite that appear to be pseudomorphic after andalusite (Fig. 6h). A sample in the interdigitated contact-zone contains Sil + Bt + Grt(l), in which garnet and sillimanite textures are similar to those in rocks upgrade of the staurolite-out isograd in area D (Fig. 6f). The metamorphic field-gradient for area K is interpreted to be the same as that for areas D, E and J (Fig. 8a).

Area L: eastern side of the northern part of the tail (*Fig. 1*)

Metapelitic lithologies are rare in area L. Rocks within 350 m of the contact contain Sil + Bt + Grt (this study and Leclair 1988). Sillimanite occurs both as fibrolitic masses and in coarse aggregates intergrown with biotite, the latter resembling those seen at high grade in area D (Fig. 6f). Inclusions of fibrolitic sillimanite within garnet indicate late-stage growth of garnet. Although there is not sufficient information from these few assemblages to constrain a metamorphic field-gradient for area L, it seems likely that the pressure of area L was at least as high as that in areas D, E, J and K, and possibly higher, given the overall tilt of the batholith (more discussion below).

Area M: the Bonnington Pluton (*Fig. 1*)

In area M, fine-grained Crd + Bt assemblages were found at a maximum distance of 600 m from the northern contact of the Bonnington Pluton. The cordierite porphyroblasts are <1 mm in size and completely altered. Assemblages of Crd + Bt containing fresh cordierite were found at the western end of the east–west-trending septum between the northern and southern lobes of the Bonnington Pluton (Fig. 1). The abundance of cordierite and the lack of andalusite in area M indicate low-pressure conditions, like in area A (Fig. 8a).

INTERPRETATION OF SEQUENCES OF MINERAL ASSEMBLAGES

Figure 9 is a synthesis of the dominant assemblages in the Nelson aureole, with a focus on the pressure-sensitive intermediate-grade assemblages involving cordierite, andalusite and staurolite. The mineral-assemblage symbols in Figure 9 are representative of the most abundant intermediate-grade assemblages in each area.

The systematic distribution of the mineral assemblages around the aureole is striking. There is no overlap between staurolite-bearing and cordierite-bearing assemblages; the former occur exclusively in the eastern part of the aureole, and the latter occur exclusively in the western part of the aureole and at its southern and northern tips, as well as in the aureole of the Bonnington Pluton. Between the domains of Crd ± And and St ± And assemblages is a narrow domain 2–3 km wide in which andalusite-only assemblages are dominant. The lines defining the boundaries of the mineral-assemblage domains have been drawn in the simplest way to be consistent with the available constraints, but involve considerable extrapolation through areas devoid of data and may mask complexities.

A line separating domains where And + Kfs or Ms + Sil are stable [corresponding to the bathograd separating bathozones 1 and 2 of Carmichael (1978) and facies series 1 and 2a of Pattison & Tracy (1991)] has also been plotted approximately in Figure 9 on the basis of the few available constraints in the northern part of the aureole. This line occurs within the Crd ± And domain. No areas containing staurolite-bearing assemblages develop And + Kfs. The line separating domains in which there is evidence for partial melting in high-grade K-feldspar-bearing assemblages (areas B, I and D), *versus* those in which there is no evidence for partial melting (area G), corresponds approximately with the line separating Crd ± And assemblages from andalusite-only assemblages.

Considering that Crd ± And and St ± And assemblages may form under the same pressure conditions in rocks showing relatively modest variations in bulk Mg/(Fe + Mg) (Fig. 3c), the mutually exclusive development of these assemblages suggests that the range of bulk composition of the argillaceous metapelites around the aureole is small, in agreement with the whole-rock and biotite compositions plotted in Figure 2a. This point is made further in Figure 2b, in which the whole-rock and biotite compositions are grouped according to mineral assemblage. There is substantial compositional overlap between different mineral-assemblages, indicating that bulk-composition variation is not the primary determinant of the distribution of the mineral assemblages in the aureole. The mineral-assemblage patterns are therefore interpreted to be primarily due to the effects of small variations in pressure.

Figure 8b shows how the mineral-assemblage domains of Figure 9 correlate with pressure-dependent domains in P–T space defined by key subassemblages [in Carmichael's (1978) terminology, bathozones], with the dashed mineral-assemblage boundaries in Figure 9 corresponding to the dashed boundaries between bathozones in Figure 8b [in Carmichael's (1978) terminology, bathograds]. The sequences of mineral assemblages within the bathozones correspond closely with the facies series of Pattison & Tracy (1991) (Fig. 8b) and partially with bathozones 1–4 of Carmichael (1978) [see Pattison & Tracy (1991) and Pattison (2001) for a comparison and discussion].

Of note is the absence of Ms + St + Crd + Bt assemblages, supporting the contention of Pattison *et al.* (1999) that this is not a stable association in most if not all bulk compositions. The narrow andalusite-only domain in Figure 9 corresponds to the small bathozone in Figure 8b that separates lower-pressure cordierite-bearing assemblages from higher-pressure staurolite-bearing assemblages. Pattison & Tracy (1991) did not identify a separate facies-series corresponding to this bathozone because of a lack of natural examples, and included it in their facies series 2a (Fig. 8b). This bathozone, and therefore the width of the andalusite-only domain in the field, will shrink or grow with variations in bulk composition, perhaps accounting for the poorer definition of the andalusite-only domain in the northern part of the aureole (area I, Fig. 4b) compared to the southern tail (area B, Fig. 4a). Nevertheless, this bathozone appears to be crucial in accounting for the commonly observed separation between staurolite-bearing and cordierite-bearing sequences of mineral assemblages in the Nelson aureole and in low-pressure metamorphic settings worldwide (*e.g.*, Pattison & Tracy 1991).

The highest-pressure, andalusite-free bathozone in Figure 8b, corresponding to facies series 3 of Pattison & Tracy (1991), has not been positively identified in the Nelson aureole. Whereas the few mineral-assemblages from area L in the most easterly part of the aureole are consistent with this bathozone, they are not definitive.

Distribution and significance of garnet

The distribution of early-formed garnet, Grt(e), supports the above inferences about pressure because garnet stability increases with pressure. Grt(e) occurs in less than 5% of the low-pressure (Crd ± And)-bearing samples from areas A, G, H and I, in *ca.* 15% of the intermediate-pressure (And ± Sil)-bearing samples from areas B and I, and in >75% of the higher-pressure St ± And samples from areas D, E, J and K. The overall similarity of Mg/(Mg + Fe) and whole-rock MnO content among the areas (Table 1, Appendix 1) indicates that these bulk-composition parameters are not the primary control on the overall pattern of development of Grt(e) in the aureole, leaving variation in pressure as the most likely explanation. Higher-than-average MnO may account for the sporadic development of Grt(e) in the lower-pressure areas (*e.g.*, areas A, B and G), and lower-than-average MnO may account for the absence of Grt(e) in some rocks in the higher-pressure areas (*e.g.*, areas D, J and K) (see Fig. 4a).

Garnet Grt(e) in the lower- and intermediate-pressure areas is generally richer in Mn + Ca ($0.25 < X_{\mathrm{Mn+Ca}} < 0.44$) than Grt(e) in the higher-pressure areas ($0.16 < X_{\mathrm{Mn+Ca}} < 0.29$, omitting anomalously Mn-rich sample 03–CW–5a) (Table 1, Appendix 4). The reaction that most likely formed Grt(e) from the low-grade (Ms + Chl + Bt + Qtz)-bearing argillites is:

$$\mathrm{Ms + Chl + Qtz = Grt + Bt + H_2O.} \qquad (7)$$

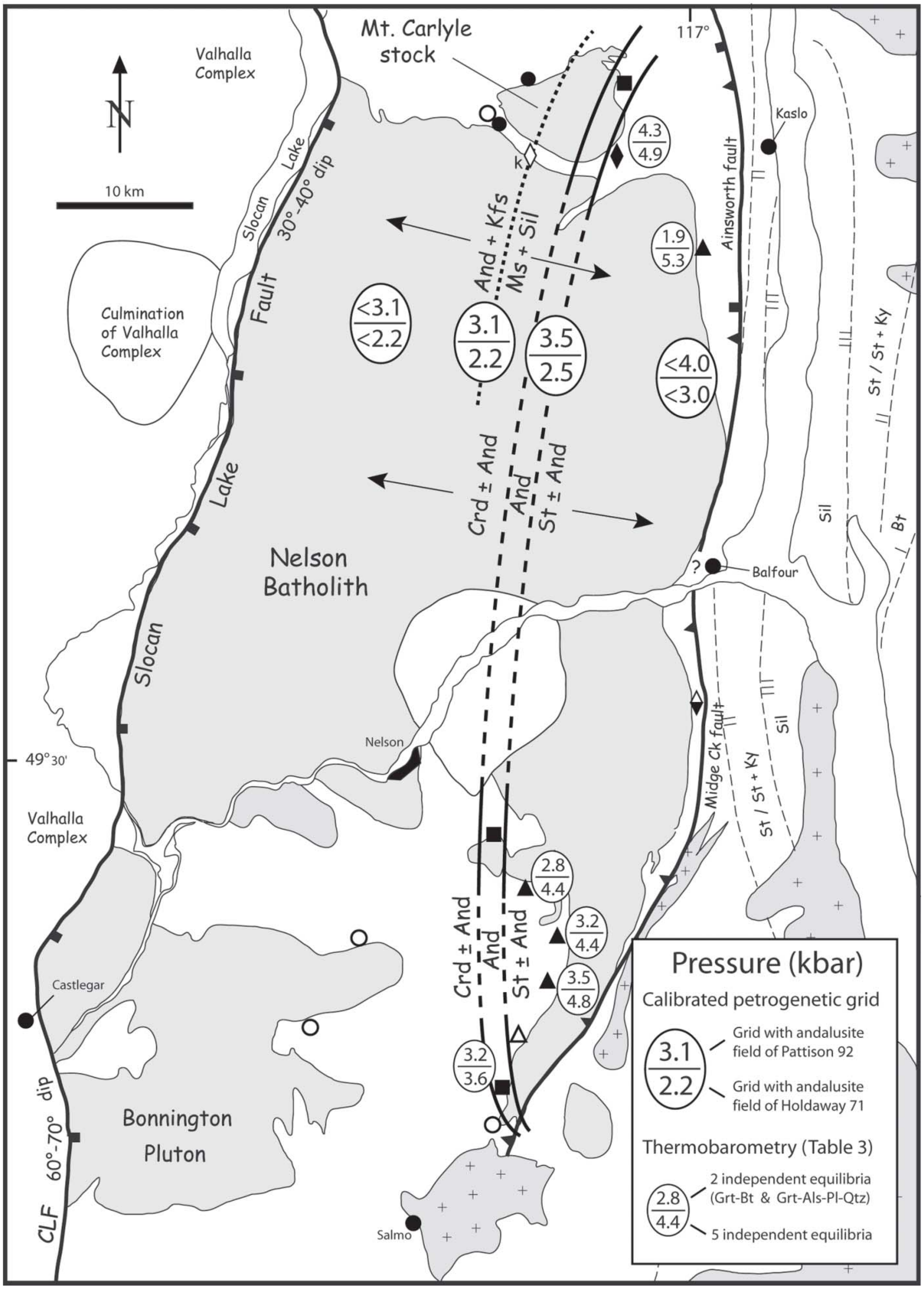
Mt. Carlyle stock
Valhalla Complex
N
10 km
117°
Kaslo
4.3
4.9
K
Slocan Lake
30°-40° dip
Ainsworth fault
And + Kfs
Ms + Sil
1.9
5.3
Culmination of Valhalla Complex
Fault
<3.1
<2.2
3.1
2.2
3.5
2.5
<4.0
<3.0
St / St + Ky
Lake
Crd ± And
And
St ± And
Sil
Bt
Nelson Batholith
?
Balfour
Slocan
Nelson
49°30'
Midge Ck fault
St / St + Ky
Sil
Valhalla Complex
2.8
4.4
3.2
4.4
3.5
4.8
Crd ± And
And
St ± And
Castlegar
3.2
3.6
Bonnington Pluton
CLF
60°-70° dip
Salmo
Pressure (kbar)
Calibrated petrogenetic grid
3.1
2.2
Grid with andalusite field of Pattison 92
Grid with andalusite field of Holdaway 71
Thermobarometry (Table 3)
2.8
4.4
2 independent equilibria (Grt-Bt & Grt-Als-Pl-Qtz)
5 independent equilibria

In the KFMASH system, reaction 7 occurs at too high a pressure to be intersected by any reasonable bulk-composition in the Nelson aureole (Fig. 3). Figure 10 shows how garnet formation by reaction 7 is expanded to lower pressures where Mn + Ca contents of the garnet in the Nelson aureole are taken into account. The calculations were performed in the MnKFMASH system, with X_{Mn} assumed to take account of the combined X_{Mn+Ca} of the natural garnet, a reasonable first-order approximation considering the low Ca contents of the natural garnet ($X_{ca} \leq 0.05$). Because reaction 7 is divariant in KFMASH, the Mg/(Mg + Fe) of chlorite is fixed at a value of 0.46, the same as that of the average whole-rock composition of the Nelson aureole (see below). For both the higher- and lower-pressure ranges in the aureole, the predicted values of X_{Mn} in garnet (0.19–0.23 and 0.26–0.29, respectively) are consistent with the measured values of X_{Mn+Ca} above. Figure 10 also shows that there is potentially a very small temperature-interval between initial formation of garnet by reaction 7 and initial formation of staurolite by reaction 3 (or, if garnet is not significantly involved, by reaction 10), consistent with the narrow to non-existent garnet zone in area D.

THERMODYNAMICALLY CALCULATED PHASE-RELATIONS

Chemical system

The chemical system chosen for thermodynamic modeling of the Nelson assemblages is the KFMASH system. This relatively simple chemical system is satisfactory in accounting for the stability of the key mineral-assemblages in this study (those involving cordierite, staurolite, chlorite, biotite, andalusite and sillimanite) because the thermodynamic stability of the mineral assemblages is only modestly affected by the small concentrations of the minor components Ca, Na, Mn, Zn and Ti in the constituent minerals (*e.g.*, Mahar *et al.* 1997, Tinkham *et al.* 2001). A possible exception is Ti, which is a significant component of biotite (Appendix 2) and might be expected to affect its stability. However, White et al. (2000) showed that the stability fields of biotite-bearing mineral assemblages in the system KFMASH + TiO_2 + Fe_2O_3 have the same topology and only slightly different absolute positions compared to those in KFMASH. Another exception may be the combination of Mn and Zn in staurolite, as discussed in more detail below.

FIG. 9. Distribution of the key intermediate-grade mineral assemblages in areas A–M of the Nelson aureole (Fig. 1), with a focus on the most abundant assemblage in each area. The mineral-assemblage domains correspond to the bathozones in Figure 8b. Mineral-assemblage symbols are the same as in Figure 4. Pressures of the bathograds are described in the text. Thermobarometry pressures come from Table 3.

The above arguments do not pertain to garnet which, as noted above, contains significant Mn and Ca and is stabilized at low pressure by these components. Our observations suggest that the type of garnet that occurs in the majority of the Nelson assemblages, Grt(e), formed at low grade and persisted up-grade as a more or less passive phase, showing little change in its grain size or euhedral to subhedral habit from lower grade (*e.g.*, Figs. 5c, 6a, c, e). In particular, there is little evidence for dissolution of Grt(e), including in the abundant staurolite-bearing rocks in which garnet dissolution is expected by reaction 3 (see Fig. 10). Whereas we do not suggest that Grt(e) was wholly chemically inert and therefore completely uninvolved in reactions involving the other porphyroblasts, we argue that it does not appear to have been a significant modal participant. We therefore treat garnet as an additional or "extra" phase stabilized by the non-KFMASH components Mn and, to a lesser degree, Ca.

Support for our treatment of garnet comes from Symmes & Ferry (1992), Mahar *et al.* (1997) and Wei *et al.* (2004), who showed that garnet occurs as a ubiquitous "extra" phase in metapelites above a pressure-dependent threshold of whole-rock MnO content (*ca.* 0.1 wt% MnO at 3 kbar). Mahar *et al.* (1997) and Wei *et al.* (2004) showed that the addition of MnO as a component and garnet as a phase has virtually no effect on the calculated stability of mineral assemblages in KFMASH below 5 kbar for a metapelite composition nearly identical to the average bulk-composition of the Nelson aureole [compare Figs. 3a and 3b of Mahar *et al.* (1997) and Figs. 5a and 5b of Wei *et al.* (2004)].

Pressure–temperature diagrams

Figure 11 shows P–T mineral-assemblage stability diagrams ("pseudosections") for our bulk compositions, calculated using two different thermodynamic datasets: (1) the Holland & Powell (1998) dataset, and (2) the Spear, Pattison & Cheney (unpublished) thermodynamic dataset, reported in Pattison *et al.* (2002), hereafter referred to as the "Spear *et al.* dataset". The diagrams were calculated using the Gibbs software of Spear (1988, 1990) and Spear *et al.* (2001). A silicate melt phase was not included in the calculations, but the approximate position of the "wet granite" solidus is shown. Above the solidus, dehydration reactions become dehydration-melting reactions that produce silicate liquid instead of an H_2O-rich volatile phase, and have a steeper slope in P–T space.

Three Nelson bulk-compositions are modeled in Figure 11: the average of the 18 out of 24 compositions that plot below the Grt–Chl tie line in Figure 2 [henceforth referred to as the average Nelson bulk-composition: A = 0.1; Mg/(Mg + Fe) = 0.46], and the Fe-richest and Mg-richest extremes of the same population [A = 0.1; Mg/(Mg + Fe) = 0.4 and 0.5, respectively]. The average sample of the Nelson aureole contains, in weight percent, SiO_2 60.41, TiO_2 0.93, Al_2O_3 20.10, FeO 5.68, MnO 0.08, MgO 2.30, CaO 1.06, Na_2O 1.53, K_2O 4.17, P_2O_5 0.15, LOI 3.09.

We have chosen to emphasize the lower-Al compositions because compositions that plot above the Grt–Chl tie line are predicted to develop a range of low-grade, biotite-free mineral assemblages involving some or all of chloritoid, staurolite, andalusite or kyanite (*e.g.*, Reche *et al.* 1998, Spear *et al.* 2001), for which there is no evidence. Instead, low-grade samples outside the aureole contain biotite without other porphyroblasts. The apparently Al-rich composition of the samples that plot above the garnet–chlorite tie line may be due to some or all of unrepresentative sampling, deficiencies in the projection scheme, or removal of alkalis from the rocks in association with fluid release during prograde metamorphism (*e.g.*, Ague 1991). Evidence in support of removal of alkalis as a general process comes from the relatively high average A value of

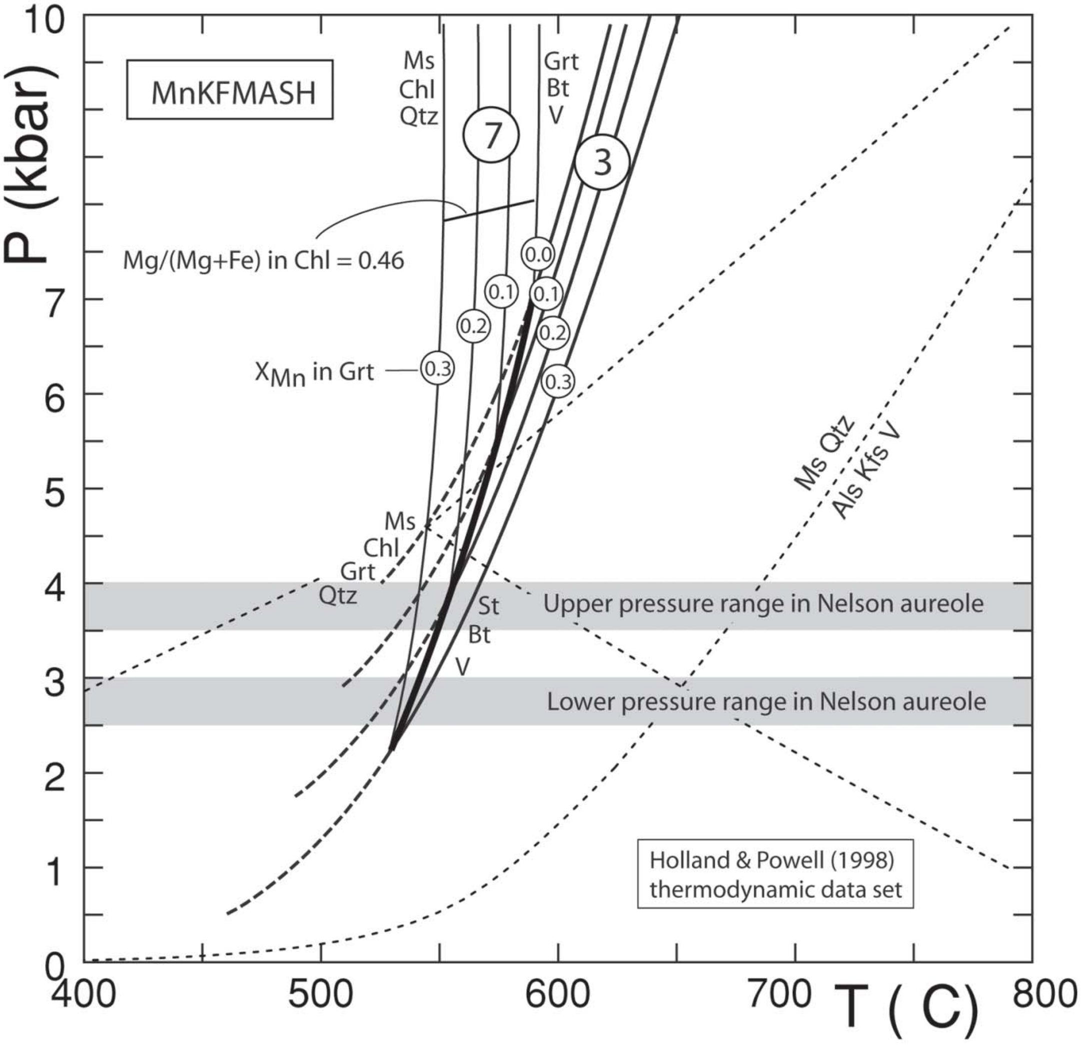

FIG. 10. Calculated displacement of reactions 3 and 7 with varying X_{Mn} in garnet, illustrating the expansion of garnet stability to low pressure as X_{Mn} increases. The value of Mg/(Mg + Fe) in chlorite in reaction 3 is fixed at a value of 0.46, the same as the average whole-rock composition in the aureole. Calculations were performed using the Gibbs method of Spear *et al.* (2001) with the Holland & Powell (1998) thermodynamic dataset. The triple point is taken from Pattison (1992). The higher and lower ranges of pressure come from Figures 9 and 11. See text for further discussion.

the porphyroblastic Nelson samples (0.17) compared to the A value of average subgreenschist- and greenschist-grade metapelite from Ague (1991) (–0.04 and –0.02, respectively, using the same projection scheme).

Figure 11a is calculated for the average Nelson bulk-composition using the Spear *et al.* dataset, whereas Figure 11b is calculated for the same bulk-composition using the Holland & Powell dataset. The average Nelson bulk-composition, converted to KFMASH to give an A value of 0.1 (in which A = $Al_2O_3 – 3K_2O$) and Mg/(Mg + Fe) of 0.46, is, in wt%, SiO_2 63.13, Al_2O_3 16.70, FeO 5.06, MgO 2.40, K_2O 4.70, H_2O 8.00. In Figure 11a, the diagram is calculated for a fluid of variable $a(H_2O)$ in equilibrium with graphite, appropriate for the graphite-bearing Nelson samples. Figure 11b is calculated assuming $a(H_2O) = 1$, but this does not affect the topology of the reactions, which is the focus of the discussion below. Figures 11c and d are calculated for the Fe-richer and Mg-richer bulk-compositions using the Spear *et al.* dataset in equilibrium with graphite.

Solid lines representing the sequences of mineral assemblages from areas A, B and D, the best-documented areas in the aureole, have been placed on Figure 11. Examining Figures 11a and 11b, neither diagram satisfies all the mineral-assemblage constraints. Figure 11a accounts well for the sequences of mineral assemblages from areas A and B if it is assumed that the metamorphic field-gradients are isobaric, a reasonable assumption in a contact aureole (more discussion below). An isobaric metamorphic field-gradient that largely satisfies the staurolite-bearing sequence of assemblages in area D can be plotted (dashed line), except that it occurs in the stability field of sillimanite rather than andalusite. No St + And field is predicted in Figure 11a in KFMASH. If, however, the measured amounts of Mn and Zn in the natural staurolite [average (Mn + Zn)/(Mn + Zn + Fe + Mg) = 0.06 for area D] are taken into account, the stability field of St + Al_2SiO_5 in Figure 11a is displaced to lower pressure by 200–400 bars (depending on assumptions about Mn and Zn partitioning among staurolite, chlorite and biotite), closer to the stability field of andalusite. The dashed metamorphic field-gradient for area D in Figure 11a has therefore been lowered by the minimum amount required for it to enter the stability field of andalusite (solid line). A small field of stability of St + And, such as in Figure 11a, appears to be at odds with the significant width of the St + And field in the field (*e.g.*, area D in Fig. 4a) but, as noted above, staurolite persists well up-grade of where it starts to react out, suggestive of sluggish kinetics of reaction. The total range of pressure between areas A and D is inferred to be about 1 kbar.

The P–T diagram in Figure 11b, calculated from the Holland & Powell (1998) dataset, can only accommodate the sequences of mineral assemblages of areas A and B if the metamorphic field-gradients involve significant pressure increase (in the case of area A, a pressure increase of *ca.* 1 kbar, equivalent to *ca.* 3 km depth, over the <1 km width of the aureole). We consider such metamorphic field-gradients to be unreasonable geologically. The slope of these metamorphic field-gradients is largely controlled by the positive slope of reaction 14, which Pattison *et al.* (2002) argued should have a gentle negative slope, like that in Figure 11a. As in Figure 11a, there is no stability field for St + And in KFMASH, a problem that is not apparently solved by calculation of the phase equilibria in MnKFMASH (compare Figs. 5a and 5b of Wei et al. 2004). However, the problem is largely diminished if the larger field of stability of andalusite proposed by Pattison (1992) is used rather than the one in Figure 11b that is based on Holdaway (1971) (Johnson *et al.* 2003: dotted line in Fig. 11b), and if, in addition, the effects of Zn in staurolite are taken into account.

Overall, we consider the topology of Figure 11a to be a better model of the observed relationships than the topology of Figure 11b. Other features that favor Figure 11a over 11b include predicted partitioning of Fe and Mg between staurolite and garnet that agrees with what is found in nature (garnet more Fe-rich than staurolite, *e.g.*, Table 1), and an AFM topology of cordierite, chlorite and biotite in which chlorite lies on the Mg-rich side of the Crd–Bt tie line (for a summary of the natural evidence, see Pattison 1987). The topology of Figure 11a is preserved if a modified version of the Spear *et al.* dataset, based on the Holdaway (1971) triple point instead of the Pattison (1992) triple point, is used (see Fig. 10 of Pattison *et al.* 2002).

Figures 11c and d show the effect of varying whole-rock Mg/(Mg + Fe) on the stabilities of the mineral assemblages. For the bulk composition richer in Fe (Fig. 11c), there is a small field of stability for St + And even without taking account of Mn and Zn in staurolite. For the bulk composition richer in Mg (Fig. 11d), the sequence of mineral assemblages in area D would be predicted to be like that observed in area B. A stability field for andalusite-free Ms + Crd + Kfs assemblages (reaction 15) is predicted at low pressure for the Mg-rich bulk composition, consistent with the local development of these assemblages in area G.

Temperature–$X_{Fe–Mg}$ diagrams

Figure 12 shows isobaric T–$X_{Fe–Mg}$ diagrams for 3.0, 3.5 and 4.0 kbar, corresponding to the isobaric lines in Figures 11a, c and d. Two types of T–$X_{Fe–Mg}$ diagram for each pressure are shown in Figure 12: one type shows mineral-assemblage stability (Figs. 12a, c and e), and the other, mineral compositions (Figs. 12b, d and f).

In Figures 12a, c, and e, the range of Nelson whole-rock compositions is shown as the vertical grey band. Representative mineral-assemblage symbols for areas A, B and D also are shown, with the measured whole-rock Mg/(Mg + Fe) compositions of the labeled symbols coming from Table 1. These diagrams show how the stability fields of Crd ± And, And-only and St ± And

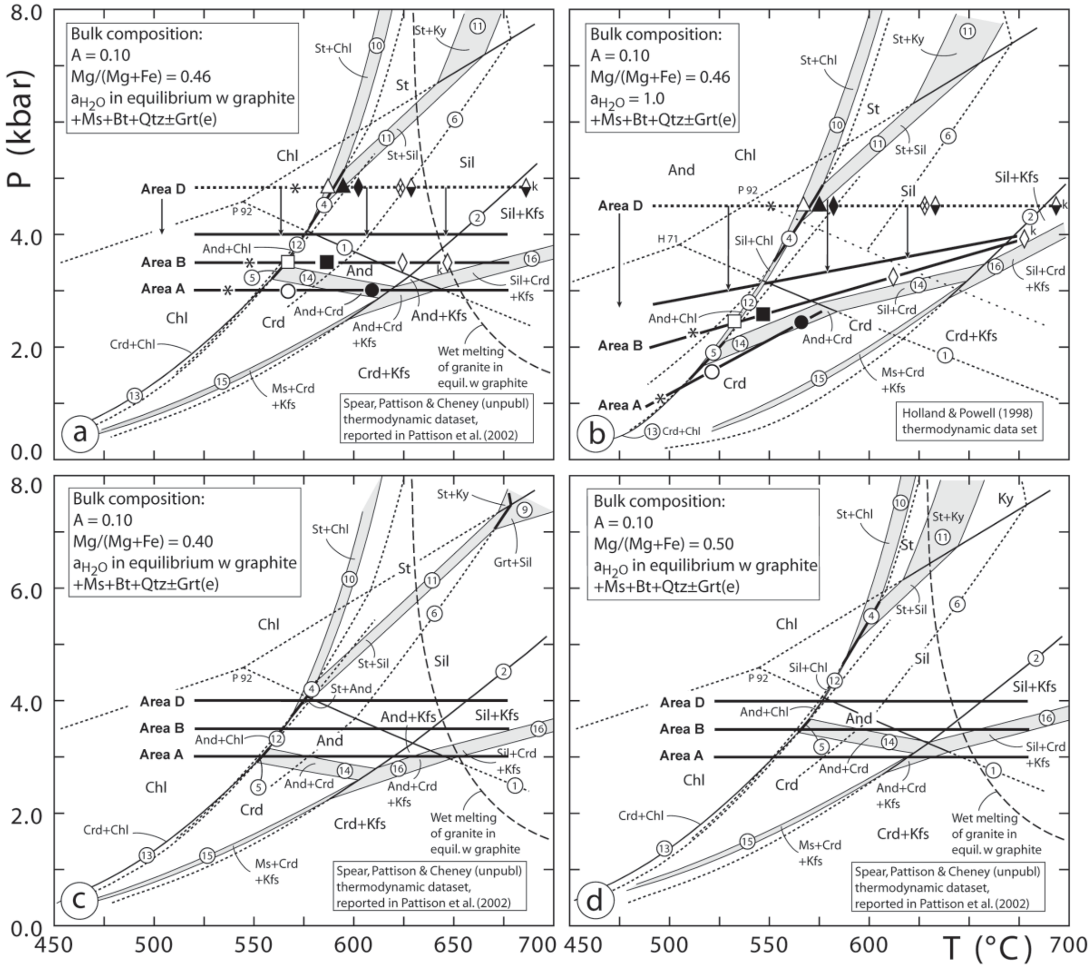

FIG. 11. Calculated P–T mineral-assemblage stability diagrams in KFMASH for Nelson whole-rock compositions, calculated using the Gibbs software of Spear *et al.* (2001). Numbered reactions are given in Table 2. Dashed portions of numbered reactions are not "seen" by the bulk composition of interest. The solid isobaric lines correspond to the isobaric T–$X_{Fe–Mg}$ diagrams in Figure 12. P 92: Al_2SiO_5 triple point of Pattison (1992). The "wet melting" curve in equilibrium with graphite comes from Cesare *et al.* (2003). (a) Diagram calculated using the Spear, Pattison & Cheney (unpublished) thermodynamic dataset, reported in Pattison *et al.* (2002), with $a(H_2O)$ in equilibrium with graphite. The bulk composition is the average composition of the Nelson metapelites. Isobaric metamorphic field-gradients and representative mineral-assemblages for areas A, B and D are shown (symbols listed in Fig. 4). See text for discussion of the dashed and solid isobaric lines for area D. (b) Diagram for the same bulk-composition as in Figure 11a calculated using the Holland & Powell (1998) thermodynamic dataset with $a(H_2O) = 1.0$. H 71: Al_2SiO_5 triple point of Holdaway (1971). Dotted line labeled P 92: And = Sil reaction from Pattison (1992). Metamorphic field-gradients that satisfy the mineral-assemblage sequences from areas A, B and D are shown (see text for discussion). (c) Same as Figure 11a, except calculated for the bulk composition richer in Fe. (d) Same as Figure 11a, except calculated for the bulk composition richer in Mg.

assemblages become displaced to more Mg-rich compositions and therefore sweep through the Nelson bulk-composition band as pressure rises. Significantly different sequences of mineral assemblages are predicted to occur for relatively small variations in pressure, consistent with the observations in the aureole. In Figure 12e, the predicted field of stability of St + And barely intersects the bulk-composition band. The shaded domains between dashed lines show approximately how the St + And stability field should be expanded to make

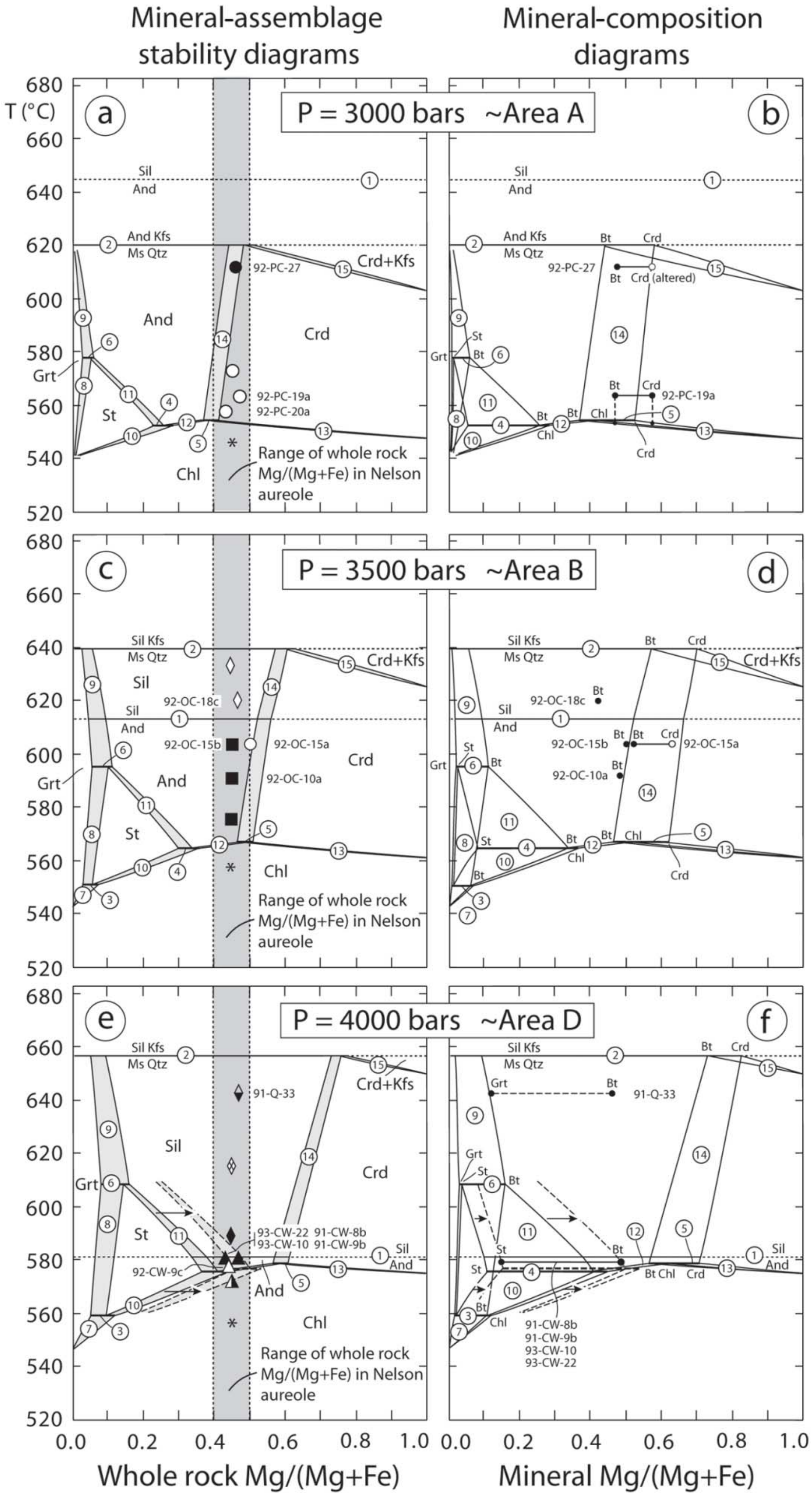

FIG. 12. Calculated isobaric T–X_{Fe-Mg} diagrams in KFMASH for 3.0, 3.5 and 4.0 kbar, corresponding to the isobaric lines in Figures 11a, c and d.. Diagrams were calculated using the Gibbs software of Spear *et al.* (2001) for an A value of 0.1. Numbered reactions are given in Table 2. Dashed portions of reactions are not "seen" by the bulk composition of interest. (a), (c), (e): Mineral-assemblage stability diagrams. The range of Nelson whole-rock compositions is shown as the vertical grey band between Mg/(Mg + Fe) = 0.4 and 0.5. Representative assemblages and measured bulk-compositions from areas A, B and D are shown (symbols are listed in Fig. 4 and bulk-composition data are provided in Appendix 1 and Table 1). In (e), staurolite-bearing stability fields barely intersect the range of Nelson compositions in KFMASH. Shaded domains between dashed lines are an estimate of where these fields should lie to satisfy the observed assemblages of minerals. (b), (d), (f): Diagrams showing calculated Mg/(Mg + Fe) value of minerals in the domains of Figure 12a, c and e. Measured compositions of minerals from the labeled samples are shown for comparison. In (b) and (d), the open-circle symbols are for altered cordierite, whose composition is estimated. In (f), the calculated compositions of staurolite and biotite in KFMASH are richer in Fe than the measured compositions. Arrows point to dashed lines that show where the mineral-composition lines should lie to satisfy the measured compositions.

the calculated phase-relations fit with observed assemblages in area D. Some of this expansion may be accounted for by the effects of Mn and Zn in staurolite, as discussed above.

In the mineral-composition diagrams, measured compositions from the labeled samples allow comparison with the predicted compositions. Those from areas A and B (Figs. 12b, d) fit reasonably well with the measured compositions, but as with Figure 12e, the predicted compositions of the staurolite-bearing samples from area D are more Fe-rich than the measured compositions. The dashed lines in Figure 12f show approximately where the predicted compositional contours involving staurolite-bearing assemblages should lie to satisfy the measured compositions.

Assignment of Pressures to Bathograds

With the exception of staurolite, the calculated phase-diagrams in Figures 11a and 12 largely satisfy the phase relations and mineral compositions in the aureole. We have therefore used these diagrams to assign absolute pressures to the bathograds in Figure 8 and 9. Using the facies-series notation of Pattison & Tracy (1991) in Figure 8b, the facies series 1/2a bathograd is the intersection of reactions 1 and 2 [the same as bathograd 1/2 of Carmichael (1978)]. The 2a/2b bathograd, which corresponds to the boundary between andalusite-only and staurolite-bearing assemblages, is not as precisely defined because of the issues surrounding the thermodynamic stability of staurolite, and the dependence of staurolite stability on relatively small variations in whole rock Mg/(Mg + Fe) (compare Figs. 11a, c and d). The 2b/3 bathograd is the intersection of reactions 1 and 4. Owing to a lack of definitive assemblages, the 2b/3 bathograd cannot be located in the aureole, although area L on the eastern edge of the batholith contains assemblages permissive of facies series 3. For this reason, we treat the pressure of the 2b/3 bathograd as a maximum for the St + And assemblages in the eastern part of the aureole.

Two sets of pressures for these bathograds are shown in Figures 8 and 9. The higher set of pressures (3.1, 3.5 and 4.0 kbar, respectively) comes from Figure 11a of this study and is based on the Pattison (1992) triple point, whereas the lower set of pressures (2.2, 2.5 and 3.0 kbar, respectively) comes from Figure 10d of Pattison *et al.* (2002) and is based on the Holdaway (1971) triple point. Recent studies seem to favor the larger field of stability of andalusite proposed by Pattison (1992) (*e.g.*, Spear *et al.* 1999, Tinkham *et al.* 2001, Johnson *et al.* 2003, Cesare *et al.* 2003, Clarke *et al.* 2004). The pressure differences between the bathograds are about the same using either dataset. The total difference in pressure between bathograds 1/2a and 2b/3 is less than 1 kbar, showing that the mineral assemblages are remarkably sensitive discriminants of small differences in pressure within the stability field of andalusite.

Comparison with Thermobarometry

Thermobarometry of aureole rocks

Six representative samples from around the aureole were selected for thermobarometric analysis using the "optimal thermobarometry" approach of Powell & Holland (1994). The results were obtained from the "average P–T method" using the Holland & Powell (1998) thermodynamic dataset and activity–composition models (May 14, 2001 update). The results are listed in Table 3 and plotted in Figure 9. An illustration of the uncertainty accompanying the P–T estimates for a single sample, 91–Q–33 from area D, is provided in Figure 13. Mineral compositions used in all calculations are listed in Appendices 2–7. To make comparisons among samples uniform, the same subset of mineral end-members was used for all samples.

The results vary depending on the number and choice of end members. Results from "traditional" thermobarometry, involving intersection of the temperature-sensitive garnet–biotite equilibrium and pressure-sensitive garnet – Al_2SiO_5 – plagioclase – quartz equilibrium (the "2 independent equilibria" estimates of Table 3 and Fig. 13), are scattered and show no correlation with the mineral-assemblage patterns in Figure 9, although the mean value for the six samples, 3.1 kbar, falls within the expected range of pressure in the aureole. Increasing the number of end members, and therefore independent equilibria, makes the system algebraically overdetermined and amenable to the statistical treatment described by Powell & Holland (1994). The "fit" parameter of Powell & Holland (1994) is minimized for selections of end members giving four or five independent equilibria (Table 3). There is a significant reduction in the size of the error ellipse if the five independent equilibria option is adopted, suggesting that this might be the best method. Although the relative pressures using this option fit reasonably with the pressure differences implied by the mineral assemblages (Fig. 9), the mean absolute value for the six samples, 4.6 kbar, is outside the stability field of andalusite.

A significant point, shown graphically in Figure 13, is the considerable uncertainty in the thermobarometry. For this one sample, individual estimates of pressure, using different sets of end members, span a range of 1.5 kbar, whereas the uncertainty on each of these estimates, as represented by the shaded 1σ uncertainty ellipses, is at least ±1.1 kbar (Table 3). The combined uncertainty for this one sample is more than double the range in pressure represented by all of the sequences of mineral assemblages in the aureole. We therefore consider that thermobarometry is too insensitive to provide any refinement of the pressure constraints from the mineral assemblages, and if applied in isolation, could lead to erroneous conclusions.

HORNBLENDE GEOBAROMETRY OF THE INTRUSIVE ROCKS

Figure 14 shows pressures from Al-in-hornblende geobarometry of the intrusive rocks based on the analytical data in Table 1 of Ghent *et al.* (1991). Pressures from two different calibrations are shown: the Johnson & Rutherford (1989) calibration used by Ghent *et al.* (1991), and the Anderson & Smith (1995) calibration that takes account of temperature variation. The mean pressure is the same using the two calibrations, 4.6 kbar, but individual samples can yield significantly different results.

Apart from consistently low pressures in the Bonnington Pluton that fit quite well with the aureole constraints, there is little spatial pattern to the pressures in the Nelson batholith using either calibration. The 4.8–6.4 kbar pressures in the center of the batholith obtained using the Johnson & Rutherford (1989) calibration are reduced to 3.3–5.5 kbar using the Anderson & Smith (1995) calibration, even though some of these samples contain what is interpreted to be magmatic epidote, indicative of high pressures of crystallization (Ghent *et al.* 1991). Many samples yield pressures that are considerably above the aureole pressure, and there can be sharp differences in pressure between closely spaced samples (*e.g.*, the two samples to the immediate southwest of the city of Nelson, Fig. 14).

Although it is beyond the scope of this paper to explore the full implications of these findings, the possibility that some of the analyzed hornblende records crystallization at depths other than the level of emplacement seems likely. If hornblende crystallized at a range of depths between the levels of magma generation and magma emplacement, the low-pressure end of the range of hornblende-derived pressures may provide the best estimate of the level of emplacement. Several pressures

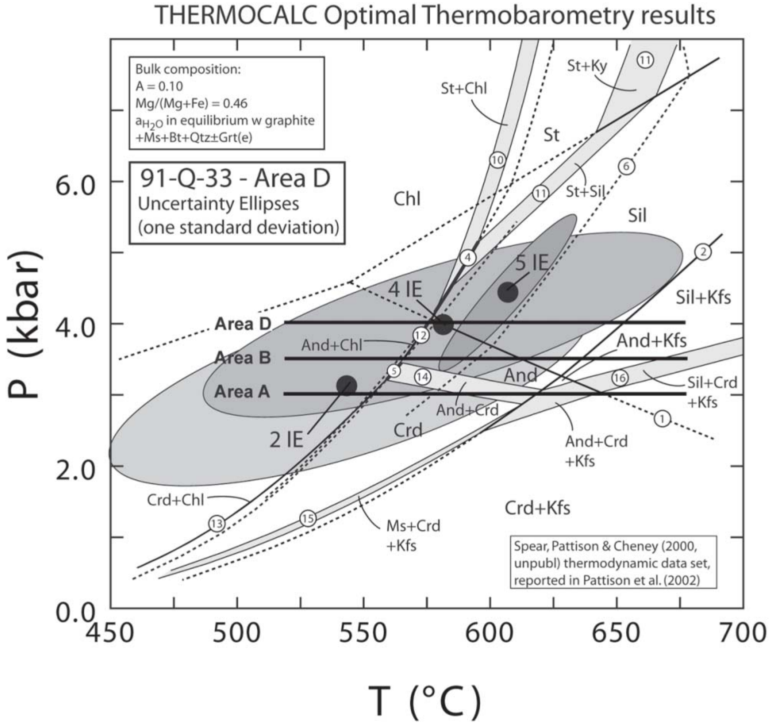

FIG. 13. P–T results for sample 91–Q–33 (area D) from multi-equilibrium “Optimal thermobarometry” (Powell & Holland 1994), using the “average P–T” method. The stability fields of mineral assemblages and isobaric metamorphic field-gradients from Figure 11a are shown for comparison. Details of the P–T results are provided in Table 3 and are discussed in the text. The error ellipses are for one standard deviation of uncertainty based on estimates in Powell & Holland (1994). “2 IE”, “4 IE” and “5 IE”: error ellipses based on 2, 4 and 5 independent equilibria (Table 3). The solid dots at the center of each ellipse are the best estimate of the P–T condition for that set of equilibria.

TABLE 3. PRESSURE–TEMPERATURE RESULTS RELEVANT TO ASSEMBLAGES IN THE AUREOLE OF THE NELSON BATHOLITH, BRITISH COLUMBIA, CALCULATED USING THE "OPTIMAL THERMOBAROMETRY" APPROACH OF POWELL & HOLLAND (1994)

Area	Sample	Assemblage	System components	End members	#	Als	P kbar	sd (P)	T °C	sd T	Corr	Fit
B	92-OC-18c	Sil-And-Grt(e)	CFMAS(K+H)*	alm, py, gr, ann, phl, an, q, als	2[§]	Sil	3.2	1.5	533	98	0.68	n.a.
			CFMAS(K+H)	Above + mu	3	Sil	2.7	1.3	529	97	0.74	0.54
			CFMAS(K+H)	Above + east	4	Sil	2.9	1.2	540	95	0.72	0.47
			CKNFMASH	Above + pa, ab, H_2O	5	Sil	3.6	1.2	653	39	0.90	0.74
			CKNFMASH	Above + cel	6	Sil	4.6	1.6	682	51	0.88	1.34
D	92-CW-22	St-And-Grt(e)	CFMAS(K+H)*	alm, py, gr, ann, phl, an, q, als	2[§]	And	3.5	1.7	525	91	0.73	n.a.
			CFMAS(K+H)	Above + mu	3	And	4.4	1.2	549	95	0.67	0.60
			CFMAS(K+H)	Above + east	4	And	4.5	1.2	556	87	0.66	0.51
			CKNFMASH	Above + pa, ab, H_2O	5	And	4.8	1.1	596	31	0.93	0.50
			CKNFMASH	Above + cel	6	And	5.0	1.1	602	30	0.93	0.64
D	91-Q-33	Sil-Grt(l)	CFMAS(K+H)	alm, py, gr, ann, phl, an, q, als	2[§]	Sil	3.2	1.4	543	95	0.69	n.a.
			CFMAS(K+H)	Above + mu	3	Sil	3.9	1.3	556	96	0.76	0.98
			CFMAS(K+H)	Above + east	4	Sil	4.0	1.3	565	94	0.74	0.73
			CKNFMASH	Above + pa, ab, H_2O	5	Sil	4.4	1.1	613	30	0.91	0.66
			CKNFMASH	Above + cel	6	Sil	4.7	1.1	621	29	0.91	0.83
E	92-A-2c	St-And-Grt(e)	CFMAS(K+H)	alm, py, gr, ann, phl, an, q, als	2[§]	And	2.8	1.4	465	80	0.73	n.a.
			CFMAS(K+H)	Above + mu	3	And	3.7	1.1	490	78	0.68	0.75
			CFMAS(K+H)	Above + east	4	And	3.8	1.1	495	78	0.67	0.58
			CKNFMASH	Above + pa, ab, H_2O	5	And	4.4	1.1	593	31	0.93	0.82
			CKNFMASH	Above + cel	6	And	4.6	1.1	598	31	0.93	0.85
J	NB-52	St-And-Sil -Grt(e)	CFMAS(K+H)	alm, py, gr, ann, phl, an, q, als	2[§]	Sil	4.3	1.6	527	93	0.70	n.a.
			CFMAS(K+H)	Above + mu	3	Sil	4.3	1.4	527	93	0.77	0.04
			CFMAS(K+H)	Above + east	4	Sil	4.4	1.4	537	91	0.75	0.26
			CKNFMASH	Above + pa, ab, H_2O	5	Sil	4.9	1.2	596	29	0.93	0.42
			CKNFMASH	Above + cel	6	Sil	5.1	1.2	599	28	0.93	0.46
K	91-FL-1b	Sil-Grt(l)	CFMAS(K+H)	alm, py, gr, ann, phl, an, q, als	2[§]	Sil	1.9	2.0	577	102	0.49	n.a.
			CFMAS(K+H)	Above + mu	3	Sil	4.9	3.2	604	211	0.73	1.97
			CFMAS(K+H)	Above + east	4	Sil	4.9	2.1	608	143	0.70	1.39
			CKNFMASH	Above + pa, ab, H_2O	5	Sil	5.3	1.7	661	43	0.93	1.17
			CKNFMASH	Above + cel	6	Sil	5.8	1.6	672	41	0.93	1.16
All	Average		CFMAS(K+H)	alm, py, gr, ann, phl, an, q, als	2[§]	A/S	3.2	1.6	528	93	0.67	n.a.
			CFMAS(K+H)	Above + mu	3	A/S	4.0	1.6	543	112	0.72	0.81
			CFMAS(K+H)	Above + east	4	A/S	4.1	1.4	550	98	0.71	0.66
			CKNFMASH	Above + pa, ab, H_2O	5	A/S	4.6	1.2	619	34	0.92	0.72
			CKNFMASH	Above + cel	6	A/S	5.0	1.3	629	35	0.92	0.88

All assemblages contain Ms + Qtz + Bt + Pl. Grt(e): early garnet, Grt(l): late garnet. Mineral end-member abbreviations are those of Powell & Holland (1994). sd(P), sd(T): one standard deviation on pressure and temperature. Corr, Fit: discussed in Powell & Holland (1994) and in this paper. #: Number of independent equilibria. * The ratio of K : H is fixed in all relevant (mica) end-members, so that K + H represents a single system component. [§] The intersection of Grt–Bt thermometer and the Grt–Als–Pl–Qtz barometer. Because the P–T intersection is exactly determined, the "fit" parameter does not pertain (n.a.: not applicable). Mineral compositions used in the calculations are listed in the Appendices. Garnet-rim compositions are used. For FL–1b, in which muscovite was not analyzed, muscovite from 91–Q–33 (same mineral assemblage) was used. Software used for these calculations: THERMOCALC (Powell & Holland 1988), release 3.2. Thermodynamic dataset: Holland & Powell (1998; May 14, 2001 release). Activity–composition formulations: program AX (Holland & Powell 1998; May 7, 2001 release).

fall within the 3–4 kbar range, consistent with the aureole constraints, although they do not indicate the tilting seen in Figure 9. Our results suggest that great care is required in the use of hornblende barometry to determine depths of pluton emplacement and post-intrusion tilting, and that analysis of the contact aureole is likely to give better results.

Regional Tectonic Implications

The mineral-assemblage domains (bathozones) in Figure 9 are interpreted to represent the intersection of isobaric surfaces, frozen into the rocks at the time of emplacement of the Nelson Batholith, with the present-day topographic surface. These have a dominantly north–south trend, with an indication of a gentle concave-to-the-east curvature, recognizing that the lack of constraints between areas F and G (Fig. 1) could mask greater complexity in the map pattern of the bathozones. The deepest levels of exposure occur on the eastern side of the main batholith, and shallower levels of exposure occur on the western side of the batholith, northeast of the main body and near the southern tip of the tail adjacent to the Bonnington Pluton. These patterns indicate

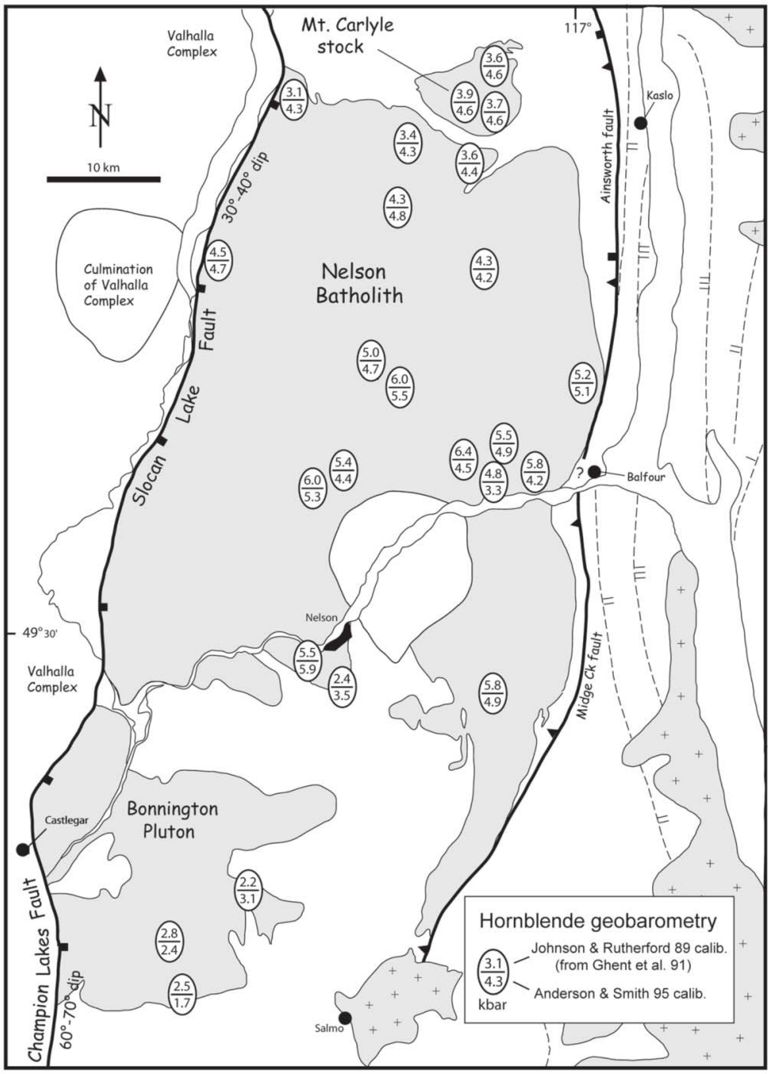

FIG. 14. Pressures from hornblende geobarometry of the intrusive rocks (compare with Fig. 9).

a predominantly westward tilt of the batholith and aureole.

Using the 2b/3 bathograd from Figure 8b as a maximum limit on pressure on the east side of the batholith, a pressure difference of *ca.* 1.0 kbar can be inferred between the eastern edge of the batholith and area G, where bathograd 1/2 is inferred to occur (Fig. 9). This is equivalent to a depth difference of 3–4 km over a horizontal east–west distance of *ca.* 20 km. The resultant tilt is 8–11° to the west, although it could be less and may not be uniform across the whole batholith. The westward tilt of the Nelson Batholith is consistent with the suggestion by Ghent *et al.* (1991) that the floor of the batholith is exposed near the West Arm of Kootenay Lake, where the granite contact dips shallowly westward. Although the evidence for tilting of the batholith apparently contradicts the assumption that the metamorphic field-gradient in the different parts of the aureole was isobaric (*e.g.*, Fig. 8a), in practice the inferred 8–11° tilt results in a depth difference of only 150–250 m across the observed widths of the aureole (1.0–1.5 km), corresponding to a negligible difference in pressure of 0.05–0.08 kbar.

The regional tilts defined by the contact-metamorphic assemblages are interpreted to be due to some combination of eastward thrusting of the Nelson Batholith over crust-scale ramps during Cretaceous–Paleocene shortening and Eocene east-side-down normal motion on the listric Slocan Lake – Champion Lakes fault system (Ghent *et al.* 1991) (Fig. 9). East-side-down normal motion would lead to west-side-down tilting of the Nelson Batholith in the hanging wall. However, the region of maximum displacement on this fault system (10–20 km) is located near the Valhalla culmination (Carr *et al*. 1987), diminishing southward to zero at latitude 49° N and northward to zero a few kilometers north of Slocan Lake (*ca.* 15 km north of the northern margin of the map in Fig. 9) (Simony & Carr 1997). If tilting of the batholith were due entirely to normal faulting and if the isobaric surfaces prior to faulting were horizontal, the map pattern of the bathograds would be notably convex to the east. This pattern is not observed, suggesting that the earlier contractional tectonism exerted a significant control on the tilting.

During thrusting of Quesnellia onto the North American continental margin, the Nelson Batholith and aureole rode passively in the upper plate of deep-seated thrust faults linked to more easterly contractional structures. A possible explanation for the westward tilt of the batholith is that it presently sits above a west-dipping frontal ramp, with the subtle concave-eastward map pattern of the isobars resulting from the batholith having been situated between two inward-facing lateral ramps, forming a scoop that was later inverted by thrusting over the frontal ramp. Such a ramp geometry has been interpreted from seismic data by Varsek & Cook (1994). The 8–11° westward tilt in the eastern half of the batholith may provide a crude estimate of the dip of the frontal thrust-ramp, although this is likely a maximum, because the later Eocene east-side-down normal motion on the Slocan Lake – Champion Lakes fault may have steepened the tilt in the region of maximum normal motion opposite the Valhalla culmination.

ACKNOWLEDGEMENTS

We acknowledge Dugald Carmichael for his inspiration in focusing on the systematics of assemblages of metamorphic minerals, and for his detailed review of this paper, which led to many changes, although perhaps not as many as he would have liked. We thank Tim Johnson, Robert Raeside and Marc St-Onge for their formal reviews that led to significant tightening of the paper, Robert Martin for his editing, and Doug Tinkham for advice on phase equilibria. Helen Tomkins, Andy Tomkins and Neil Windom provided much appreciated assistance in the field, and Helen Tomkins carried out some of the whole-rock analyses. Philip Simony provided support to JJV from his NSERC Discovery Grant and invaluable advice on tectonic interpretations. DRMP acknowledges NSERC Discovery Grant 0037233 for the support of this research.

REFERENCES

AGUE, J.J. (1991): Evidence for major mass transfer and volume strain during regional metamorphism of pelites. *Geology* **19**, 855-858.

ANDERSON, J.L. & SMITH, D.R. (1995): The effects of temperature and fO_2 on the Al-in-hornblende barometer. *Am. Mineral.* **80**, 549-559.

ARCHIBALD, D.A., GLOVER, J.K., PRICE, R.A., FARRAR, E. & CARMICHAEL, D.M. (1983): Geochronology and tectonic implications of magnetism and metamorphism, southern Kootenay Arc and neighbouring regions, southeastern British Columbia. I. Jurassic to Cretaceous. *Can. J. Earth Sci.* **20**, 1891-1913.

__________, KROGH, T.E., ARMSTRONG, R.L. & FARRAR, E. (1984): Geochronology and tectonic implications of magnetism and metamorphism, southern Kootenay Arc and neighbouring regions, southeastern British Columbia. II. Mid-Cretaceous to Eocene. *Can. J. Earth Sci.* **21**, 567-583.

BEDDOE-STEPHENS, B. (1981): Metamorphism of the Rossland volcanic rocks, southern British Columbia. *Can. Mineral.* **19**, 631-641.

BROWN, D.A. & LOGAN, J.M. (1988): Geology and mineral evaluation of Kokanee Glacier Provincial Park, southeastern British Columbia. *In* Geologic Fieldwork 1987. *B.C. Ministry Energy Mines Petrol. Res., Pap.* **1988–1**, 31-48.

CAIRNES, C.E. (1934): Slocan mining camp, British Columbia. *Geol. Surv. Can., Mem.* **173**.

CARMICHAEL, D.M. (1978): Metamorphic bathozones and bathograds: a measure of the depth of post-metamorphic uplift and erosion on the regional scale. *Am. J. Sci.* **278**, 769-797.

CARR, S.D., PARRISH, R.R. & BROWN, R.L. (1987): Eocene structural development of the Valhalla complex, southeastern British Columbia. *Tectonics* **6**, 175-196.

CESARE, B., MARCHESI, C., HERMANN, J. & GÓMEZ-PUGNAIRE, M.T. (2003): Primary melt inclusions in andalusite from anatectic graphitic metapelites: implications for the position of the Al_2SiO_5 triple point. *Geology* **31**, 573-576.

CHILDS, J.F. (1968): *Contact Relationships of the Mount Carlyle Stock, British Columbia.* M.Sc. thesis, University of Alberta, Edmonton, Alberta.

CLARKE, D.B. AND 35 OTHERS (2004): Occurrence and origin of andalusite in peraluminous felsic igneous rocks. *J. Petrol*. **46**, 1-32.

COOK, F.A., GREEN, A.G., SIMONY, P.S., PRICE, R.A., PARRISH, R.R., MILKEREIT, B., GORDY, P.L., BROWN, R.L., COFLIN, K.C. & PATENAUDE, C. (1988): Lithoprobe seismic reflection structure of the southeastern Canadian Cordillera: initial results. *Tectonics* **7**, 157-180.

COX, J. (1979): *The Geology of the Northwest Margin of the Nelson Batholith, British Columbia*. M.Sc. thesis, University of Alberta, Edmonton, Alberta.

CROSBY, P. (1968): Tectonic, plutonic and metamorphic history of the Central Kootenay Arc, British Columbia, Canada. *Geol. Soc. Am., Spec. Pap.* **99**.

DRYSDALE, C.W. (1917): Ymir mining camp, British Columbia. *Geol. Surv. Can., Mem.* **94**.

FYLES, J.T. (1967): Geology of the Ainsworth–Kaslo Area, British Columbia. *B.C. Dept. Mines, Bull.* **53**.

GHENT, E.D., NICHOLLS, J., SIMONY, P.S., SEVIGNY, J.H. & STOUT, M.Z. (1991): Hornblende geobarometry of the Nelson Batholith, southeastern British Columbia: tectonic implications. *Can. J. Earth Sci.* **28**, 1982-1991.

GHOSH, D.K. (1995): U–Pb geochronology of Jurassic to early Tertiary granitic intrusives from the Nelson–Castlegar area, southeastern British Columbia, Canada. *Can. J. Earth Sci*. **32**, 1668-1680.

HEDLEY, M.S. (1952): Geology and ore deposits of the Sandon area, Slocan Mining Camp, British Columbia. *B.C. Dep. Mines, Bull.* **29**.

HOLDAWAY, M.J. (1971): Stability of andalusite and the aluminum silicate phase diagram. *Am. J. Sci.* **271**, 97-131.

HOLLAND, T.J.B. & POWELL, R. (1998): An internally consistent thermodynamic data set for phases of petrological interest. *J. Metamorph. Geol.* **16**, 309-344.

JOHNSON, M.C. & RUTHERFORD, M.J. (1989): Experimental calibration of the aluminum-in-hornblende geobarometer with application to Long Valley caldera (California) volcanic rocks. *Geology* **17**, 837-841.

JOHNSON, T.E., BROWN, M. & SOLAR, G.S. (2003): Low-pressure subsolidus and suprasolidus phase equilibria in the MnNCKFMASH system: constraints on conditions of regional metamorphism in western Maine, northern Appalachians. *Am. Mineral.* **88**, 624-638.

KRETZ, R. (1983): Symbols for rock-forming minerals. *Am. Mineral.* **68**, 277-279.

LECLAIR, A.D. (1988): *Polyphase Structural and Metamorphic Histories of the Midge Creek Area, Southeast British Columbia: Implications for Tectonic Processes in the Central Kootenay Arc*. Ph.D. thesis, Queen's University, Kingston, Ontario.

LITTLE, H.W. (1960): Nelson map area, west half, British Columbia. *Geol. Surv. Can., Mem.* **308**.

MAHAR, E.M., BAKER, J.M., POWELL, R., HOLLAND, T.J.B. & HOWELL, N. (1997): The effect of Mn on mineral stability in metapelites. *J. Metamorph. Geol.* **15**, 223-238.

MCALLISTER, A.L. (1951): Ymir map area, British Columbia. *Geol. Surv. Can., Pap.* **51–4**.

NICHOLLS, J. & STOUT, M.Z. (1988): Picritic melts in Kiluaea – evidence from the 1967–1968 Halemaumau and Hiiaka eruptions. *J. Petrol.* **29**, 1031-1057.

PARRISH, R.R. (1992): U–Pb ages of Jurassic–Eocene plutonic rocks in the vicinity of the Valhalla Complex, southeastern British Columbia. *In* Radiogenic Age and Isotopic Studies: Report 5. *Geol. Surv. Can. Pap.* **91–2**, 115-134.

________, CARR, S.D. & PARKINSON, D.L. (1988): Eocene extensional tectonics and geochronology of the southern Omenica belt, British Columbia and Washington. *Tectonics* **7**, 181-212.

PATTISON, D.R.M. (1987): Variations in Mg/(Mg + Fe), F , and (Fe,Mg)Si = 2Al in pelitic minerals in the Ballachulish thermal aureole, Scotland. *Am. Mineral*. **72**, 255-272.

________ (1992): Stability of andalusite and sillimanite and the Al_2SiO_5 triple point: constraints from the Ballachulish aureole, Scotland. *J. Geol.* **100**, 423-446.

________ (2001): Instability of Al_2SiO_5 'triple point' assemblages in muscovite + biotite + quartz-bearing metapelites, with implications. *Am. Mineral.* **86**, 1414-1422.

________, SPEAR, F.S., DEBUHR, C.L., CHENEY, J.T. & GUIDOTTI, C.V. (2002): Thermodynamic modeling of the reaction muscovite + cordierite → Al_2SiO_5 + biotite + quartz + H_2O: constraints from natural assemblages and implications for the metapelitic petrogenetic grid. *J. Metamorph. Geol.* **20**, 99-18.

________, ________ & Cheney, J.Y. (1999): Polymetamorphic origin of muscovite + cordierite + staurolite + biotite assemblages: implications for the metapelitic petrogenetic grid and for P–T paths. *J. Metamorph. Geol.* **17**, 685-703.

________ & Tracy, R.J. (1991): Phase equilibria and thermobarometry of metapelites. *In* Contact Metamorphism (D.M. Kerrick, ed.). *Rev. Mineral.* **26**, 105-206.

Powell, R. & Holland, T.J.B. (1988): An internally consistent thermodynamic dataset with uncertainties and correlations. 3. Application to geobarometry methods, worked examples and a computer program. *J. Metamorph. Geol.* **6**, 173-204.

________ & ________ (1994): Optimal geothermometry and geobarometry. *Am. Mineral.* **79**, 120-133.

Reche, J., Martinez, F.J., Arboleya, M.L., Dietsch, C. & Briggs, W.D. (1998): Evolution of a kyanite-bearing belt within a HT–LP orogen: the case of the NW Variscan Iberia. *J. Metamorph. Geol.* **16**, 379-394.

Sevigny, J.H. & Parrish, R.R. (1993): Age and origin of Late Jurassic and Paleocene granitoids, Nelson Batholith, southern British Columbia. *Can. J. Earth Sci.* **30**, 2305-2314.

Simony, P.S. & Carr, S.D. (1997): Large lateral ramps in the Eocene Valkyr shear zone: extensional ductile faulting controlled by plutonism in southern British Columbia. *J. Struct. Geol*. **19**, 769-784.

Spear, F.S. (1988): The Gibbs method and Duhem's theorem: the quantitative relationships among P, T, chemical potential, phase composition and reaction progress in igneous and metamorphic systems. *Contrib. Mineral. Petrol.* **99**, 249-256.

________ (1990): Petrologic determination of metamorphic pressure – temperature – time paths. *In* Metamorphic Pressure – Temperature – Time Paths (F.S. Spear & S.M. Peacock, eds.). *28th Int. Geol. Congress, Short Course in Geology* **7**, 1-55.

________, Kohn, M.J & Cheney, J.T. (1999): P–T paths from anatectic pelites. *Contrib. Mineral. Petrol.* **134**, 17-32.

________, Pyle, J.M. & Storm, L.C. (2001): Thermodynamic modeling of mineral reactions: an introduction to Program Gibbs. *Geol. Soc. Am., Northeast Sect., Short Course* **504** (on CD).

Symmes, G.H. & Ferry, J.M. (1992): The effect of whole-rock MnO content on the stability of garnet in pelitic schists during metamorphism. *J. Metamorph. Geol.* **10**, 221-237.

Tinkham, D.K., Zuluaga, C.A. & Stowell, H.H. (2001): Metapelite phase equilibria modeling in MnNCKFMASH: the effect of variable Al_2O_3 and MgO/(MgO + FeO) on mineral stability. *Geol. Materials Res.* **3**(1), 42 p.

Varsek, J.L. & Cook, F.A. (1994): Three-dimensional crustal structure of the Eastern Cordillera, southwestern Canada and northwestern United States. *Geol. Soc. Am., Bull.* **106**, 803-823.

Vogl, J.J. (1993): *The Southern Tail of the Nelson Batholith, Southeast British Columbia: Emplacement and Deformational History*. M.Sc. thesis, Queen's University, Kingston, Ontario.

________ & Simony, P.S. (1992): The southern tail of the Nelson Batholith, southeast British Columbia: structure and emplacement. *Geol. Surv. Can., Pap.* **92–1A**, 71-76.

Wei, C.J., Powell, R. & Clarke, G.L. (2004): Calculated phase equilibria for low- and medium-pressure metapelites in the KFMASH and KMnFMASH systems. *J. Metamorph. Geol.* **22**, 495-508.

White, R.W., Powell, R., Holland, T.J.B. & Worley, B.A. (2000): The effect of TiO_2 and Fe_2O_3 on metapelitic assemblages at greenschist and amphibolite conditions: mineral equilibria calculations in the system $K_2O–FeO–MgO–Al_2O_3–SiO_2–H_2O–TiO_2–Fe_2O_3$. *J. Metamorph. Geol.* **18**, 497-512.

Received October 22, 2003, revised manuscript accepted October 12, 2004.

APPENDIX 1. RESULTS OF WHOLE-ROCK ANALYSES OF SAMPLES FROM THE AUREOLE OF THE NELSON BATHOLITH, BRITISH COLUMBIA

Area	SU	#	SiO_2	TiO_2	Al_2O_3	FeO	MnO	MgO	CaO	Na_2O	K_2O	P_2O_5	BaO	Ce	Cu	Zn	LOI	Total	C	S	A	Mg#	X_{Mn}	X_{Ca}
A	Ym	92–PC–20a	60.52	0.94	21.21	4.62	0.08	1.56	0.23	1.43	4.69	0.09	2896	102	4	69	4.08	99.75	1.03	0.01	0.180	0.424	0.011	0.082
A	Ym	92–PC–19a	61.48	1.06	20.54	4.46	0.08	1.87	0.42	1.73	4.39	0.15	1695	103	18	55	3.34	99.70	0.49	0.07	0.137	0.487	0.012	0.118
A	Ym	92–PC–17	61.13	1.14	21.39	4.06	0.10	1.51	0.38	0.81	4.81	0.14	2060	148	25	36	3.93	99.62	0.82	0.09	0.235	0.470	0.017	0.206
A	Ym	92–PC–27	61.18	0.85	19.08	5.71	0.13	2.39	0.50	1.02	4.62	0.16	1753	86	57	143	3.83	99.67	0.95	0.22	0.023	0.463	0.014	0.213
B	Ym	92–OC–15a	48.74	1.37	30.50	4.24	0.07	1.67	0.66	1.53	5.86	0.21	4519	152	27	26	4.47	99.79	0.62	0.05	0.424	0.497	0.012	0.192
B	Ym	92–OC–9	65.60	0.55	17.83	4.06	0.10	2.20	1.64	2.34	2.02	0.27	1379	77	43	42	3.08	99.84	1.72	0.01	0.268	0.491	0.013	0.279
B	Ym	92–OC–4	53.62	1.25	23.86	6.24	0.49	2.02	1.49	1.76	3.73	0.13	1537	130	30	83	4.93	99.71	1.49	0.04	0.287	0.413	0.054	0.319
B	Ym	92–OC–17	60.29	0.92	19.88	5.27	0.18	2.16	1.30	1.25	3.82	0.13	1714	117	74	84	3.80	99.20	1.37	0.74	0.149	0.465	0.022	0.365
B	Ym	92–OC–18c	50.49	1.16	26.16	5.54	0.11	2.21	3.12	4.91	3.04	0.10	987	102	8	125	2.88	99.84	1.40	0.01	0.123	0.467	0.014	0.260
B	Ym	03–OC–2b	68.22	0.82	16.53	5.07	0.09	2.04	0.57	0.69	3.14	0.12	1401	78	44	38	2.24	99.68	0.54	0.08	0.227	0.456	0.011	0.313
D	Ym	93–CW–23	64.72	0.83	17.53	5.65	0.08	1.74	0.74	0.76	3.57	0.18	1402	98	66	90	3.69	99.65	1.22	0.22	0.176	0.387	0.010	0.350
D	Ym	93–CW–22	63.41	0.82	18.25	6.71	0.10	2.25	0.31	0.67	3.47	0.11	1510	77	118	108	3.54	99.83	0.70	0.06	0.238	0.402	0.010	0.204
D	Ym	91–CW–9c	58.22	0.94	21.18	5.76	0.09	2.16	0.57	0.97	5.99	0.14	2137	100	37	104	3.13	99.38	0.65	0.11	-0.262	0.439	0.010	0.245
D	Ym	93–CW–10	63.35	0.91	19.13	5.97	0.08	2.02	0.73	1.20	3.08	0.13	1207	100	5	110	2.93	99.66	1.00	0.01	0.285	0.411	0.009	0.252
D	Ym	93–CW–14a	64.98	0.92	18.83	5.27	0.11	1.94	0.89	0.57	3.31	0.14	1336	77	32	118	2.72	99.83	0.63	0.22	0.291	0.438	0.014	0.463
D	Ym	91–Q–33	62.34	0.87	18.01	6.50	0.10	3.00	2.28	1.56	3.23	0.20	658	95	47	76	1.69	99.85	0.04	0.01	-0.002	0.483	0.009	0.447
D	Ym	93–CW–19a	63.66	0.98	18.87	5.24	0.21	2.28	0.59	0.70	4.40	0.13	2304	114	29	67	2.44	99.74	0.64	0.22	0.093	0.482	0.025	0.318
E	Ym	92–A–3a	61.60	0.90	18.89	6.82	0.09	2.85	1.03	1.02	4.19	0.17	1161	96	66	74	2.40	100.10	0.11	0.01	0.040	0.458	0.008	0.358
F	Ym	92–ER–2c	66.60	0.89	15.89	5.62	0.09	2.40	1.90	1.40	3.14	0.17	577	91	38	56	1.26	99.42	0.07	0.01	-0.072	0.470	0.010	0.429
G	Sl	92–SP–18a	58.01	0.94	22.79	4.56	0.04	2.00	0.32	1.33	5.14	0.11	3016	113	21	33	4.22	99.77	0.40	0.04	0.167	0.490	0.005	0.117
G	Sl	92–SP–18b	60.60	0.90	19.62	5.00	0.03	2.22	0.36	0.89	4.19	0.25	2024	113	94	22	4.93	99.22	1.41	0.07	0.197	0.485	0.004	0.183
J	Sl	93–NK–1	63.09	0.89	18.75	7.38	0.08	2.42	0.75	1.59	1.56	0.14	444	80	60	129	2.77	99.49	0.31	0.03	0.366	0.396	0.008	0.207
K	Sl	92–FL–15a	60.50	0.92	19.57	6.84	0.07	2.66	1.73	1.37	3.94	0.18	493	78	49	68	1.81	99.66	0.05	0.01	0.023	0.441	0.006	0.411
K	Sl	92–FL–1b	64.52	1.07	19.46	5.93	0.04	1.98	1.03	1.35	2.16	0.11	765	108	41	70	2.05	99.80	0.47	0.01	0.379	0.415	0.005	0.297
Average			61.12	0.95	20.16	5.52	0.11	2.15	0.98	1.37	3.81	0.15	1624	101	43	76	3.17	99.68	0.76	0.10	0.166	0.451	0.013	0.276

SU: Stratigraphic unit; Ym: Ymir Group; Sl: Slocan Group. # Sample number. The FeO reported is an expression of total iron. All constituents are reported in wt%, except for BaO, Ce, Cu and Zn, reported in ppm. A: A value (molar projection) in the AFM projection; see text for details of the projection scheme. Mg#: molar ratio Mg/(Mg + Fe), after removal of Fe associated with ilmenite (see text for further details). X_{Mn} = Mn / (Mn + Fe + Mg); X_{Ca} = Ca / (Ca + Na).

APPENDIX 2. COMPOSITION OF BIOTITE FROM THE AUREOLE OF THE NELSON BATHOLITH, BRITISH COLUMBIA

Area	Sample	SiO_2	TiO_2	Al_2O_3	FeO	MnO	MgO	CaO	Na_2O	K_2O	F	H_2O	Total	Si	Al	Ti	Fe^{2+}	Mg	Mn	Ca	Na	K	Total	Mg#
A	92-PC-19a	34.55	1.33	19.70	20.12	0.09	9.78	0.03	0.13	9.67	0.57	3.65	99.38	2.64	1.78	0.08	1.29	1.12	0.01	0.00	0.02	0.94	7.87	0.46
A	92-PC-27	35.22	1.36	19.74	19.12	0.15	10.00	0.00	0.04	8.98	0.47	3.71	98.59	2.69	1.78	0.08	1.22	1.14	0.01	0.00	0.01	0.87	7.79	0.48
B	92-OC-10a	35.67	1.67	19.87	19.03	0.15	10.03	0.01	0.08	9.10	0.53	3.72	99.61	2.69	1.77	0.09	1.20	1.13	0.01	0.00	0.01	0.87	7.78	0.48
B	92-OC-15a	35.56	1.72	20.05	17.59	0.08	10.93	0.02	0.11	9.06	0.56	3.72	99.14	2.68	1.78	0.10	1.11	1.23	0.00	0.00	0.02	0.87	7.78	0.53
B	92-OC-15b	35.76	1.40	19.29	18.83	0.09	11.04	0.02	0.02	9.54	0.24	3.87	100.00	2.69	1.71	0.08	1.19	1.24	0.01	0.00	0.00	0.92	7.83	0.51
B	92-OC-18c	35.01	2.76	19.53	20.37	0.18	8.42	0.03	0.14	9.61	0.36	3.77	100.03	2.66	1.75	0.16	1.29	0.95	0.01	0.00	0.02	0.93	7.78	0.42
D	91-CW-8b	35.87	1.60	20.00	18.88	0.09	10.40	0.05	0.03	9.47	0.47	3.78	100.44	2.68	1.76	0.09	1.18	1.16	0.01	0.00	0.00	0.90	7.80	0.50
D	93-CW-22	36.54	1.59	19.69	18.69	0.09	10.14	0.07	0.31	9.46	0.07	3.99	100.61	2.72	1.73	0.09	1.17	1.13	0.01	0.01	0.04	0.90	7.79	0.49
D	91-CW-9b	35.75	1.88	20.17	18.05	0.06	10.56	0.01	0.15	9.40	0.44	3.80	100.06	2.67	1.78	0.11	1.13	1.18	0.00	0.00	0.02	0.90	7.79	0.51
D	91-CW-9c	35.32	1.79	19.72	19.78	0.10	9.41	0.01	0.17	9.18	0.31	3.80	99.43	2.68	1.77	0.10	1.26	1.06	0.01	0.00	0.02	0.89	7.79	0.46
D	93-CW-10	35.50	1.70	19.80	19.15	0.00	9.93	0.01	0.09	8.76	0.16	3.88	98.91	2.69	1.77	0.10	1.21	1.12	0.00	0.00	0.01	0.85	7.76	0.48
D	91-Q-33	35.18	2.26	19.83	19.37	0.11	9.40	0.02	0.10	9.59	0.39	3.78	99.86	2.66	1.77	0.13	1.23	1.06	0.01	0.00	0.01	0.93	7.79	0.46
E	92-A-3a	35.98	1.55	19.95	17.77	0.07	9.73	0.02	0.00	8.98	0.28	3.81	98.02	2.73	1.79	0.09	1.13	1.10	0.00	0.00	0.00	0.87	7.72	0.49
E	92-A-2c	35.31	1.59	20.25	19.70	0.05	9.48	0.07	0.20	9.10	0.26	3.84	99.74	2.67	1.80	0.09	1.25	1.07	0.00	0.01	0.03	0.88	7.79	0.46
F	92-ER-2c	35.46	1.68	19.60	18.98	0.36	9.70	0.02	0.21	8.69	0.08	3.90	98.65	2.70	1.76	0.10	1.21	1.10	0.02	0.00	0.03	0.84	7.76	0.48
G	92-SP-18a	36.26	1.52	20.54	16.43	0.07	11.37	0.01	0.23	8.48	0.17	3.94	98.96	2.70	1.81	0.09	1.02	1.26	0.00	0.00	0.03	0.81	7.73	0.55
G	92-SP-18b	35.56	1.31	19.93	17.58	0.14	10.96	0.00	0.27	8.39	0.43	3.75	98.14	2.70	1.78	0.07	1.11	1.24	0.01	0.00	0.04	0.81	7.76	0.53
G	92-SP-30c	36.09	1.87	20.79	16.61	0.05	10.79	0.01	0.08	9.64	0.55	3.77	100.02	2.68	1.82	0.10	1.03	1.20	0.00	0.00	0.01	0.91	7.77	0.54
I	92-MH-5a	35.34	1.17	20.12	21.44	0.16	8.65	0.02	0.11	8.53	0.21	3.84	99.50	2.69	1.81	0.07	1.36	0.98	0.01	0.00	0.02	0.83	7.76	0.42
I	92-MH-24	34.90	2.86	19.61	21.40	0.17	7.47	0.03	0.13	8.83	0.22	3.81	99.34	2.67	1.77	0.16	1.37	0.85	0.01	0.00	0.02	0.86	7.72	0.38
J	93-NK-1	34.57	1.68	19.92	21.45	0.00	8.78	0.07	0.11	7.60	0.37	3.72	98.11	2.66	1.81	0.10	1.38	1.01	0.00	0.01	0.02	0.75	7.72	0.42
J	NB-52	35.02	1.57	20.04	21.35	0.07	8.26	0.00	0.27	9.31	0.42	3.73	99.86	2.67	1.80	0.09	1.36	0.94	0.00	0.00	0.04	0.91	7.81	0.41
K	92-FL-15a	35.51	1.30	20.35	20.01	0.14	9.17	0.06	0.15	8.75	0.42	3.76	99.41	2.69	1.82	0.07	1.27	1.03	0.01	0.00	0.02	0.84	7.76	0.45
K	92-FL-1b	34.49	2.69	20.19	20.80	0.07	8.48	0.01	0.14	9.19	0.27	3.82	100.03	2.62	1.81	0.15	1.32	0.96	0.00	0.00	0.02	0.89	7.78	0.42
Average		35.43	1.74	19.94	19.27	0.11	9.70	0.02	0.14	9.05	0.34	3.80	99.41	2.68	1.78	0.10	1.22	1.09	0.01	0.00	0.02	0.87	7.78	0.47

Mg#: Mg / (Mg + Fe). Constituents reported in wt% and in atoms per formula unit containing 11 atoms of oxygen.

APPENDIX 3. COMPOSITION OF MUSCOVITE FROM THE AUREOLE OF THE NELSON BATHOLITH, BRITISH COLUMBIA

Area	Sample	SiO_2	TiO_2	Al_2O_3	FeO	MnO	MgO	CaO	Na_2O	K_2O	F	H_2O	Total	Si	Al	Ti	Fe^{2+}	Mg	Mn	Ca	Na	K	Total
B	92-OC-18c	46.06	1.65	34.17	1.29	0.01	0.79	0.01	0.37	10.72	0.10	4.43	99.56	3.08	2.69	0.08	0.07	0.08	0.00	0.00	0.05	0.92	6.97
D	91-CW-8b	46.89	0.34	36.32	1.08	0.01	0.67	0.02	0.80	10.26	0.08	4.53	100.97	3.07	2.81	0.02	0.06	0.07	0.00	0.00	0.10	0.86	6.99
D	93-CW-22	46.51	0.45	36.74	1.27	0.00	0.63	0.03	0.90	10.23	0.00	4.58	101.33	3.04	2.83	0.02	0.07	0.06	0.00	0.00	0.11	0.85	7.00
D	91-CW-9b	46.19	0.54	35.68	1.04	0.00	0.59	0.01	0.86	9.78	0.09	4.46	99.20	3.08	2.80	0.03	0.06	0.06	0.00	0.00	0.11	0.83	6.97
D	91-CW-9c	45.21	0.60	35.72	1.06	0.01	0.54	0.00	0.79	9.78	0.15	4.38	98.18	3.05	2.84	0.03	0.06	0.05	0.00	0.00	0.10	0.84	6.97
D	93-CW-10	46.09	0.49	36.03	0.89	0.01	0.47	0.02	1.09	9.08	0.00	4.49	98.66	3.07	2.83	0.03	0.05	0.05	0.00	0.00	0.14	0.77	6.94
D	91-Q-33	46.65	0.46	35.96	1.03	0.04	0.64	0.01	0.60	9.69	0.69	4.20	99.68	3.09	2.81	0.02	0.06	0.06	0.00	0.00	0.08	0.82	6.93
E	92-A-2c	46.01	0.37	36.04	1.07	0.00	0.54	0.02	0.73	9.67	0.05	4.47	98.95	3.07	2.83	0.02	0.06	0.05	0.00	0.00	0.09	0.82	6.95
J	NB-52	46.29	0.37	35.76	1.04	0.01	0.44	0.02	1.28	9.71	0.07	4.47	99.43	3.08	2.80	0.02	0.06	0.04	0.00	0.00	0.17	0.82	6.99
Average		46.21	0.59	35.82	1.09	0.01	0.59	0.02	0.82	9.88	0.14	4.45	99.55	3.07	2.81	0.03	0.06	0.06	0.00	0.00	0.11	0.84	6.97

Constituents reported in wt% and in atoms per formula unit containing 11 atoms of oxygen.

APPENDIX 4. COMPOSITION OF GARNET FROM THE AUREOLE OF THE NELSON BATHOLITH, BRITISH COLUMBIA

Area	Sample		SiO_2	TiO_2	Al_2O_3	FeO	MgO	MnO	CaO	Total	Si	Al	Ti	Fe^{2+}	Mn	Mg	Ca	Total	X_{Fe}	X_{Mg}	X_{Mn}	X_{Ca}	Mg#
A	92-PC-27	core	37.09	0.20	20.93	29.72	9.81	2.06	1.07	100.88	2.99	1.99	0.01	2.00	0.25	0.67	0.09	8.00	0.66	0.08	0.22	0.03	0.11
		rim	37.13	0.01	20.83	27.77	12.10	1.39	1.47	100.70	3.01	1.99	0.00	1.88	0.17	0.83	0.13	8.00	0.63	0.06	0.28	0.04	0.08
B	03-OC-5b	core	36.25	0.06	20.89	22.02	16.89	1.30	1.75	99.17	2.98	2.02	0.00	1.51	0.16	1.18	0.15	8.01	0.50	0.05	0.39	0.05	0.10
		rim	36.46	0.01	21.13	28.72	10.25	1.93	1.33	99.84	2.97	2.03	0.00	1.96	0.23	0.71	0.12	8.01	0.65	0.08	0.23	0.04	0.11
B	92-OC-18c	core	37.12	0.18	21.12	29.29	9.20	2.54	1.46	100.90	2.98	2.00	0.01	1.97	0.30	0.63	0.13	8.01	0.65	0.10	0.21	0.04	0.13
		rim	37.00	0.01	20.47	27.87	12.47	1.84	1.14	100.80	3.00	1.96	0.00	1.89	0.22	0.86	0.10	8.02	0.62	0.07	0.28	0.03	0.11
D	03-CW-5a	core	36.69	0.14	20.84	16.89	20.01	1.55	3.00	99.11	2.99	2.01	0.01	1.15	0.19	1.38	0.26	7.99	0.39	0.06	0.46	0.09	0.14
		rim	36.82	0.09	20.93	14.15	22.69	1.90	2.49	99.06	3.00	2.01	0.01	0.96	0.23	1.57	0.22	7.99	0.32	0.08	0.53	0.07	0.19
D	93-CW-4	core	36.95	0.08	21.08	27.85	10.67	1.83	1.86	100.32	2.99	2.01	0.00	1.88	0.22	0.73	0.16	8.00	0.63	0.07	0.24	0.05	0.11
		rim	36.88	0.01	21.03	31.65	7.16	2.27	1.32	100.32	2.98	2.01	0.00	2.14	0.27	0.49	0.11	8.01	0.71	0.09	0.16	0.04	0.11
D	91-CW-8b	rim	37.47	0.02	20.39	31.82	7.10	2.44	2.00	101.24	3.01	1.93	0.00	2.14	0.29	0.48	0.17	8.02	0.69	0.09	0.16	0.06	0.12
D	93-CW-22	core	37.23	0.02	21.23	30.92	6.94	2.28	2.42	101.04	2.98	2.01	0.00	2.07	0.27	0.47	0.21	8.01	0.69	0.09	0.16	0.07	0.12
		rim	36.99	0.01	20.48	32.59	5.55	2.68	1.55	99.85	3.00	1.96	0.00	2.21	0.32	0.38	0.13	8.02	0.72	0.11	0.12	0.04	0.13
D	91-CW-9b	core	36.94	0.00	20.76	32.58	5.26	2.98	2.03	100.55	2.98	1.97	0.00	2.20	0.36	0.36	0.18	8.04	0.71	0.12	0.12	0.06	0.14
		rim	37.10	0.00	20.87	33.04	5.31	2.75	1.58	100.65	2.99	1.98	0.00	2.22	0.33	0.36	0.14	8.02	0.73	0.11	0.12	0.04	0.13
D	91-CW-9c	core	37.04	0.00	20.71	31.48	6.14	2.74	1.81	99.92	3.00	1.98	0.00	2.13	0.33	0.42	0.16	8.01	0.70	0.11	0.14	0.05	0.13
		rim	37.12	0.00	20.91	33.05	6.35	2.45	1.50	101.38	2.98	1.98	0.00	2.22	0.29	0.43	0.13	8.03	0.72	0.10	0.14	0.04	0.12
D	91-Q-33	core	37.77	0.04	21.62	33.93	1.79	4.59	1.84	101.58	2.97	2.01	0.00	2.23	0.54	0.12	0.16	8.02	0.73	0.18	0.04	0.05	0.19
		rim	37.05	0.00	20.91	31.81	5.76	2.54	1.67	99.74	3.00	2.00	0.00	2.16	0.31	0.40	0.14	8.00	0.72	0.10	0.13	0.05	0.12
E	92-A-3a	core	37.06	0.00	20.77	31.48	7.31	2.24	1.92	100.77	2.99	1.98	0.00	2.12	0.27	0.50	0.17	8.02	0.69	0.09	0.16	0.05	0.11
		rim	36.84	0.00	20.47	31.36	7.36	2.14	1.89	100.06	3.00	1.96	0.00	2.13	0.26	0.51	0.16	8.02	0.70	0.08	0.17	0.05	0.11
E	92-A-2c	core	37.20	0.01	20.94	32.71	5.18	2.36	2.08	100.48	3.00	1.99	0.00	2.20	0.28	0.35	0.18	8.01	0.73	0.09	0.12	0.06	0.11
		rim	37.22	0.01	21.00	33.81	4.59	2.02	1.99	100.64	3.00	2.00	0.00	2.28	0.24	0.31	0.17	8.00	0.76	0.08	0.10	0.06	0.10
I	NB-52	rim	37.27	0.01	21.12	34.22	4.74	2.14	1.19	100.69	3.00	2.01	0.00	2.30	0.26	0.32	0.10	8.00	0.77	0.09	0.11	0.03	0.10
J	92-FL-1b	core	37.51	0.04	20.19	37.11	1.59	3.33	0.73	100.50	3.02	1.92	0.00	2.50	0.40	0.11	0.06	8.02	0.81	0.13	0.04	0.02	0.14
		rim	37.33	0.01	20.06	37.14	1.59	3.00	0.73	99.86	3.03	1.92	0.00	2.52	0.36	0.11	0.06	8.01	0.82	0.12	0.04	0.02	0.13
Average			37.12	0.03	20.81	30.76	7.49	2.48	1.74	100.43	3.00	1.98	0.00	2.07	0.30	0.51	0.15	8.01	0.68	0.10	0.17	0.05	0.13

X_i = i / (Fe + Mg + Mn + Ca), Mg# = Mg / (Mg + Fe), cation ratios. Constituents reported in wt% and in atoms per formula unit containing 12 atoms of oxygen.

APPENDIX 5. COMPOSITION OF STAUROLITE FROM THE AUREOLE OF THE NELSON BATHOLITH, BRITISH COLUMBIA

Area	Sample		SiO_2	TiO_2	Al_2O_3	FeO	MnO	MgO	ZnO	H_2O	Total	Si	Al	Ti	Fe^{2+}	Mg	Mn	Zn	H	Total	X_{Zn}	X_{Mn}	Mg#
D	91-CW-8b	rim	27.75	0.42	54.39	12.56	0.34	1.34	0.49	2.16	99.45	3.86	8.91	0.04	1.46	0.28	0.04	0.05	2.00	16.64	0.03	0.02	0.16
D	93-CW-22	core	28.06	0.52	56.15	12.72	0.33	1.44	0.39	2.21	101.82	3.81	8.98	0.05	1.44	0.29	0.04	0.04	2.00	16.65	0.02	0.02	0.17
		rim	27.70	0.51	55.99	12.58	0.29	1.29	0.38	2.19	100.93	3.79	9.03	0.05	1.44	0.26	0.03	0.04	2.00	16.64	0.02	0.02	0.15
D	91-CW-9b	core	28.08	0.51	56.00	13.03	0.31	1.23	0.14	2.20	101.50	3.82	8.98	0.05	1.48	0.25	0.04	0.01	2.00	16.64	0.01	0.02	0.14
		rim	27.89	0.57	55.53	12.83	0.30	1.23	0.18	2.19	100.71	3.82	8.97	0.06	1.47	0.25	0.03	0.02	2.00	16.63	0.01	0.02	0.15
D	91-CW-9c	core	27.38	0.48	55.70	12.47	0.42	1.13	0.43	2.17	100.18	3.78	9.06	0.05	1.44	0.23	0.05	0.04	2.00	16.65	0.02	0.03	0.14
		rim	27.99	0.59	55.94	11.43	0.37	1.03	1.52	2.19	101.06	3.82	9.01	0.06	1.31	0.21	0.04	0.15	2.00	16.61	0.09	0.03	0.14
E	92-A-3a	core	27.95	0.49	55.55	11.66	0.43	1.07	1.37	2.19	100.70	3.84	8.99	0.05	1.34	0.22	0.05	0.14	2.00	16.62	0.08	0.03	0.14
		rim	27.68	0.51	55.27	11.36	0.41	0.98	1.43	2.17	99.80	3.83	9.02	0.05	1.31	0.20	0.05	0.15	2.00	16.61	0.09	0.03	0.13
E	92-A-2c	rim	28.04	0.41	53.57	13.00	0.19	1.30	n.a.	2.14	98.65	3.92	8.84	0.04	1.52	0.27	0.02	n.a.	2.00	16.62	n.a.	0.01	0.15
J	93-NK-1	core	27.82	0.52	55.98	13.43	0.29	1.29	0.44	2.21	101.98	3.78	8.97	0.05	1.53	0.26	0.03	0.04	2.00	16.68	0.02	0.02	0.15
		rim	27.97	0.46	55.79	12.83	0.29	1.28	0.49	2.20	101.31	3.82	8.98	0.05	1.46	0.26	0.03	0.05	2.00	16.65	0.03	0.02	0.15
J	NB-52	rim	26.94	0.28	55.03	13.96	0.20	1.11	n.a.	2.16	100.18	3.74	9.02	0.03	1.62	0.23	0.02	n.a.	2.00	16.72	n.a.	0.01	0.12
K	92-FL-15a	rim	27.28	0.27	54.02	12.77	0.42	1.23	2.34	2.15	100.48	3.80	8.87	0.03	1.49	0.26	0.05	0.24	2.00	16.73	0.12	0.02	0.15
Average			27.75	0.47	55.35	12.62	0.33	1.21	0.80	2.18	100.63	3.82	8.97	0.05	1.45	0.25	0.04	0.08	2.00	16.65	0.04	0.02	0.15

X_i = i / (Fe + Mg + Mn + Zn), Mg# = Mg / (Mg + Fe), cation ratios. Constituents reported in wt% and in atoms per formula unit containing 23 atoms of oxygen.

APPENDIX 6. COMPOSITION OF CORDIERITE FROM THE AUREOLE OF THE NELSON BATHOLITH, BRITISH COLUMBIA

Area	Sample	SiO_2	TiO_2	Al_2O_3	FeO	MnO	MgO	CaO	Na_2O	K_2O	Total	Si	Al	Ti	Fe^{2+}	Mn	Mg	Ca	Na	K	Total	Mg#
A	92-PC-19a	48.09	0.00	32.94	7.91	0.26	6.52	0.02	0.51	0.08	96.31	5.05	0.00	4.08	0.69	0.02	0.97	0.00	0.08	0.01	10.91	0.58
G	92-SP-30c	48.96	0.00	33.89	7.21	0.22	8.89	0.01	0.20	0.00	99.37	4.97	0.00	4.05	0.61	0.02	1.32	0.00	0.03	0.00	11.00	0.68

Mg#: Mg/(Mg + Fe). Constituents reported in wt% and in atoms per formula unit containing 18 atoms of oxygen.

APPENDIX 7. COMPOSITION OF PLAGIOCLASE FROM THE AUREOLE OF THE NELSON BATHOLITH, BRITISH COLUMBIA

Area	Sample	SiO_2	Al_2O_3	FeO	MgO	CaO	Na_2O	K_2O	BaO	Total	Si	Al	Fe	Mg	Ca	Na	K	Ba	Total	X_{Ca}	X_{Na}	X_K
B	92-OC-18c	62.01	24.07	0.09	0.00	5.26	8.69	0.12	0.03	100.27	2.74	1.26	0.00	0.00	0.25	0.75	0.01	0.00	5.00	0.25	0.74	0.01
D	93-CW-22	60.59	25.55	0.19	0.00	6.26	7.89	0.12	0.00	100.60	2.68	1.33	0.01	0.00	0.30	0.68	0.01	0.00	5.00	0.30	0.69	0.01
D	91-Q-33	56.07	27.82	0.13	0.00	9.86	6.44	0.05	0.02	100.39	2.52	1.47	0.00	0.00	0.47	0.56	0.00	0.00	5.03	0.46	0.54	0.00
E	92-A-2c	57.23	27.33	0.18	0.00	9.23	6.75	0.06	0.02	100.80	2.55	1.44	0.01	0.00	0.44	0.58	0.00	0.00	5.02	0.43	0.57	0.00
J	NB-52	63.62	23.56	0.15	0.00	4.56	9.49	0.04	0.02	101.44	2.78	1.21	0.01	0.00	0.21	0.80	0.00	0.00	5.02	0.21	0.79	0.00
K	92-FL-1b	61.04	24.82	0.09	0.00	6.02	8.60	0.07	0.01	100.65	2.70	1.29	0.00	0.00	0.29	0.74	0.00	0.00	5.02	0.28	0.72	0.00

X_{Ca} = Ca / (Ca + Na + K), X_{Na} = Na / (Ca + Na + K), X_K = K / (Ca + Na + K), cation ratios. Constituents reported in wt% and in atoms per formula unit containing 8 atoms of oxygen.